Carpio, J., Prieto, J. L. & Vera, M. (2016). A local anisotropic adaptive algorithm for the solution of low-Mach transient combustion problems. *Journal of Computational Physics, 306*, 19–42.

A local anisotropic adaptive algorithm for the solution of low-Mach transient combustion problems

Jaime Carpio*, Juan Luis Prieto

Departamento de Ingeniería Energética, E.T.S. Ingenieros Industriales
Universidad Politécnica de Madrid, 28006 Madrid, Spain

Marcos Vera

Departamento de Ingeniería Térmica y de Fluidos
Universidad Carlos III de Madrid, 28911 Leganés, Spain

Abstract

A novel numerical algorithm for the simulation of transient combustion problems at low Mach and moderately high Reynolds numbers is presented. These problems are often characterized by the existence of a large disparity of length and time scales, resulting in the development of directional flow features, such as slender jets, boundary layers, mixing layers, or flame fronts. This makes local anisotropic adaptive techniques quite advantageous computationally. In this work we propose a local anisotropic refinement algorithm using, for the spatial discretization, unstructured triangular elements in a finite element framework. For the time integration, the problem is formulated in the context of semi-Lagrangian schemes, introducing the semi-Lagrange-Galerkin (SLG) technique as a better alternative to the classical semi-Lagrangian (SL) interpolation. The good performance of the numerical algorithm is illustrated by solving a canonical laminar combustion problem: the flame/vortex interaction. First, a premixed methane-air flame/vortex interaction with simplified transport and chemistry description (Test I) is considered. Results are found to be in excellent agreement with those in the literature, proving the superior performance of the SLG scheme when compared with the classical SL technique, and the advantage of using anisotropic adaptation instead of uniform meshes or isotropic mesh refinement. As a more realistic example, we then conduct simulations of non-premixed hydrogen-air flame/vortex interactions (Test II) using a more complex combustion model which involves state-of-the-art transport and chemical kinetics. In addition to the analysis of the numerical features, this second example allows us to perform a satisfactory comparison with experimental visualizations taken from the literature.

Keywords: Lagrange-Galerkin schemes, finite element method, anisotropic refinement, transient combustion problems, flame/vortex interaction.

1. Introduction

The analysis of reactive flows is a well-established field of research with a major impact in modern society [1]. This topic covers, in particular, the combustion of fossil fuels, which still produce over 85% of the world energy supply, a figure that is expected to grow in the next several decades in spite of the recent advances accomplished in electricity generation from renewable energy sources.

---

*Corresponding author

Email addresses: jaime.carpio@upm.es (Jaime Carpio*), juanluis.prieto@upm.es (Juan Luis Prieto), marcos.vera@uc3m.es (Marcos Vera)

To understand and quantify combustion processes, a well-posed mathematical model that translates the physics of the problem into equations is required. Although the conservation equations that govern chemically reactive flows are known since the mid-twentieth century, still today a comprehensive and general solution to those equations would be nothing short of a stupendous feat: to the built-in mathematical complexity of the Navier-Stokes equations, which describe by themselves such complex phenomena as turbulent flows [2], one should add the difficulties arising from the convection-diffusion-reaction equations describing energy and species mass conservation [3], in which the non-linear effects associated with convection and (to a lesser extent) diffusion are intertwined with the strong temperature dependence of the chemical reaction rates.

A paramount complication to the integration of the combustion equations stems from the large disparity of scales associated with the different terms that appear in the system [4]. The theoretical handling of such an arduous problem involves the use of asymptotic analysis and perturbation theory, an approach that has proved to be of invaluable help in ascertaining the qualitative behavior of combustion processes [5]. Nevertheless, the accuracy required to replicate experimental results and to acquire a thorough grasp of the phenomena at hand might only be attainable by means of numerical methods. The advent of numerical simulations and their application to the understanding and interpretation of combustion phenomena took place several decades ago, with the rise of digital computers and the development of reliable numerical methods that could efficiently handle the non-linearities inherent to convection, diffusion, and finite-rate chemical kinetics models [6].

In the current investigation we address the disparity of spatial scales found in transient combustion problems by means of an adaptive algorithm that generates locally refined meshes in which the evolving solution meets a prescribed accuracy. Although in computational fluid mechanics (and, more specifically, in numerical combustion [7]) finite difference and finite volume techniques have been historically more common [6, 8–11], the numerical method presented herein is based on a conforming finite element discretization. The reason for this lies in the ability of the proposed method to work with unstructured meshes, while its Galerkin character allows for an a posteriori error estimator that constitutes the base for error control and local mesh refinement. Alternative approaches for the numerical integration of combustion problems have also been proposed, including for instance spectral methods [12], projection methods [13], extended Lattice-Boltzmann methods [14], and wavelet-based techniques [15].

A key element to any adaptive finite element scheme is the way in which the a posteriori error indicator of the error incurred by the numerical integration of the equations is computed. Among the different available strategies, duality based techniques [16] stand out for their efficiency and reliability to produce "goal oriented adaptation", having been applied quite satisfactorily to steady laminar combustion problems [17–22]. However, the development of an efficient, time-marching adaptive algorithm that uses this methodology in such complex problems is still a hard challenge and a topic of active research [23, 24]. In time-dependent problems, more heuristic a posteriori error analysis, based on residuals of the governing equations or on jumps of the gradients of the solution between adjacent elements, have proved quite successful in combustion problems [25–27]. Error indicators were first developed for isotropic adaptation, where only the size of the element must be defined to accommodate for triangles as close to equilateral as possible [28]. This is a common feature to the literature cited so far; however, for the kind of problems we are interested in, anisotropic adaptation offers a decisive advantage in solving the smallest scales of the flow and capturing its directional features, such as slender jets, boundary layers, mixing layers, or flame fronts (see, e.g., [29] for an overview of anisotropic mesh adaptation applied to CFD computations, or [30] for anisotropic adaptation applied to high Reynolds number flows with economical CPU and storage resources). Thus, when anisotropic mesh refinement is employed, the computed error indicator must not only provide the size of the elements, but also their shape and orientation so as to define the optimal triangulation.

A feature that distinguishes the numerical methods employed in combustion problems is the treatment of the convective terms. The majority of the works concerned with the finite element simulation of combustion problems [17–27] consider an Eulerian description of the flow and use a Galerkin discretization along with streamline-diffusion upwinding terms to avoid spurious oscillations in the convection dominated region. In contrast, we propose here a mixed Lagrangian-Eulerian (also referred to as semi-Lagrangian) formulation that discretizes the convection operator explicitly following the trajectories of the fluid particles backwards in time (Lagrangian stage), whereas the diffusion-reaction terms define a parabolic problem which is solved in a fixed mesh (Eulerian stage). In addition to handling the convective terms in a numerically stable way, the semi-Lagrangian formulation has the ability to decouple the Navier-Stokes equations from the energy and species mass conservation equations. It translates the former into a linear Stokes problem (which involves velocity and pressure) and the latter into a parabolic problem (which involves the thermodynamic variables, e.g., temperature and species mass fractions). To the best of our knowledge, the application of semi-Lagrangian schemes is quite novel in combustion problems [31, 32].

A crucial point in semi-Lagrangian schemes is how to find the numerical solution of the displaced "feet of the characteristics" (or departure points) at the previous instant of time in the finite element space at hand. In this regard, a variety of procedures ensue: the "classical" semi-Lagrangian scheme, firstly developed in a finite difference context and later extended to a finite element framework by Allievi and Bermejo [33], is based on interpolation on the moved nodes of the mesh. This classical scheme has been used efficiently in local adaptive mesh refinement with both isotropic [31] and anisotropic [34] adaptation. The aim of this work is to improve the accuracy of this approach while also proposing a scheme that is more consistent with the methodology of finite elements: a variant of the Lagrange-Galerkin technique [35] (previously named Characteristic-Galerkin method in [36]) based on a Galerkin projection method. This alternative form that we term "semi-Lagrange-Galerkin" scheme [37] (or modified Lagrange-Galerkin method [38]), has been used with great success in isotropic uniform fixed meshes, providing a better accuracy than the classical semi-Lagrangian interpolation technique at a similar computational cost. In this work, we extend this technique to a local adaptive refinement framework with meshes composed of anisotropic elements.

Summarizing, in the present work we present a novel local anisotropic adaptive algorithm for the solution of transient combustion problems at low Mach and moderately high Reynolds numbers. We extend our method initially proposed in [34] for convection dominated equations to a complex multivariate problem, making use of the more accurate semi-Lagrange-Galerkin scheme to integrate the conservation equations in an anisotropic finite element framework. The structure of the paper is as follows. In Section 2 we present the numerical discretization of the combustion equations via semi-Lagrangian schemes, outlining the Lagrangian and Eulerian stages, as well as the traits of the anisotropic refinement algorithm when combustion processes are involved. In Section 3 we carry out a series of numerical experiments to demonstrate the capabilities of the numerical method in a classical benchmark combustion problem: the flame/vortex interaction. First, we consider a two-dimensional planar configuration featuring the interaction of a laminar premixed methane-air flame with a vortex pair; and then, we integrate a more realistic combustion model for non-premixed hydrogen-air flame/vortex interactions in a two-dimensional axisymmetric configuration, which enables the comparison with experimental visualizations found in the literature. Finally, some conclusions and an overview of future work are presented in Section 4.

2. Discretization of the combustion equations

The solution of a given combustion problem involves the integration of the conservation equations for chemically reacting flows with I chemical species involved in the model. These include the Navier-Stokes equations (mass and momentum conservation equations) coupled

with the conservation equations for energy and species mass fractions. In the low Mach number limit [7], these equations may be written as:

$$
\begin{cases}
\dfrac{\partial \rho}{\partial t} + \mathbf{u} \cdot \nabla \rho = -\rho \nabla \cdot \mathbf{u}, \\[2mm]
\rho \left(\dfrac{\partial \mathbf{u}}{\partial t} + \mathbf{u} \cdot \nabla \mathbf{u} \right) = -\nabla p + \nabla \cdot \left\{ \mu \left[\nabla \mathbf{u} + (\nabla \mathbf{u})^T \right] \right\}, \\[2mm]
\rho \left(\dfrac{\partial Y_i}{\partial t} + \mathbf{u} \cdot \nabla Y_i \right) = -\nabla \cdot \mathbf{j}_i + \dot{m}_i, \qquad i = 1, \ldots, I - 1, \\[2mm]
\rho c_p \left(\dfrac{\partial T}{\partial t} + \mathbf{u} \cdot \nabla T \right) = \nabla \cdot (\rho D_T c_p \nabla T) - \sum_{i=1}^{I} h_i \dot{m}_i - \left(\sum_{i=1}^{I} \mathbf{j}_i c_{pi} \right) \cdot \nabla T + \dfrac{\partial p_0}{\partial t}.
\end{cases}
\tag{1}
$$

In the above system of equations $\mathbf{u} = \{u_1, \ldots, u_d\}$ is the fluid velocity (where $d = 2, 3$ denotes the spatial dimension of the problem), p is the hydrodynamic pressure (accounting both for the spatial pressure variations and the isotropic component of the stress tensor), Y_i is the mass fraction of species i, and T is the fluid temperature. In addition, ρ is the density, μ the dynamic viscosity, c_p the specific heat at constant pressure, D_T the thermal diffusivity, and p_0 the thermodynamic pressure (which is spatially uniform in low Mach number flows, and thus remains constant in open vessels). Regarding the chemical species, h_i is the specific mass enthalpy, c_{pi} the specific heat at constant pressure, and $\mathbf{j}_i$ the mass diffusion flux of species i, while $\dot{m}_i$ stands for the net mass of species i produced per unit volume and unit time by the chemical reactions. Hence, we have $d + 1 + I$ conservation equations for the $d + 1 + I$ unknowns $\{u_1, \ldots, u_d, p, T, Y_1, \ldots, Y_{I-1}\}$, with an additional set of state equations and constitutive relations that provide the remaining variables as functions of the previous unknowns. The above equations must also be supplied with an appropriate set of initial and boundary conditions to define a well posed mathematical problem.

As can be noticed from (1), any of the conservation equations can be written as a generic convection-reaction-diffusion problem for the scalar variable $c(\mathbf{x}, t)$ according to:

$$
\begin{cases}
\dfrac{\partial c}{\partial t} + \mathbf{u} \cdot \nabla c = F(\mathbf{c}, t) & \text{in} \quad \Omega \times [0, T]; \\[2mm]
c(\mathbf{x}, 0) = c^0(\mathbf{x}) & \text{in} \quad \Omega; \\[2mm]
Bc|_{\partial \Omega} = 0 & t > 0;
\end{cases}
\tag{2}
$$

where the right-hand side $F(\mathbf{c}, t)$ represents a generic function that may depend on the unknown, vector-valued variable $\mathbf{c}(\mathbf{x}, t)$ as well as on its spatial derivatives, thereby representing the diffusion and reaction terms of the combustion equations; besides, B is a boundary operator, and $\Omega \subset \mathbb{R}^d$ is a bounded domain with sufficiently smooth boundary $\partial \Omega$.

To integrate the above system of equations we make use of a time-marching algorithm: first we divide the time interval $[0, t_f]$ into N_t subintervals each of the same size $\Delta t = t_n - t_{n-1}$, such that $N_t \Delta t = t_f$. Then, at each subinterval $I_n = (t_{n-1}, t_n]$, we build a regular, unstructured triangulation of the domain $\mathbb{T}_h^n = \{K_j \subset \mathbb{R}^d, \ 1 \leq j \leq NE_n\}$, with NE_n the number of elements in the mesh, a value that may possibly change from one time subinterval to another. Associated with this triangulation, we define the conforming finite element space V_h^n composed of continuous, piecewise polynomials of order $\leq m$ on each element $K \in \mathbb{T}_h^n$, so that the discrete solution $c_h^n(\mathbf{x})$ (short notation for $c_h(\mathbf{x}, t_n)$) at instant t_n may be written as:

$$
c_h^n(\mathbf{x}) = c_h(\mathbf{x}, t_n) = \sum_{i=1}^{N_h^n} C_i^n \varphi_i^n(\mathbf{x}),
\tag{3}
$$

where N_h^n denotes the number of mesh nodes in the triangulation $\mathbb{T}_h^n$, $\{\varphi_i^n\}$ represents the set of basis functions of V_h^n satisfying $\varphi_i^n(\mathbf{x}_j) = \delta_{ij}$ (with δ_{ij} the Kronecker delta), and C_i^n is the value of the function at the mesh node $\mathbf{x}_i$, $C_i^n = c_h^n(\mathbf{x}_i)$.

4

As previously discussed, the convection term is a well known source of numerical problems, particularly at high Reynolds numbers. We handle this term using a semi-Lagrangian scheme (in a classical or modified version, as we shall see). This scheme integrates (2) backwards in time at each time subinterval I_n along the characteristic curves $\mathbf{X}(\mathbf{x}, t_n; t)$ of the material derivative operator; here, $\mathbf{X}(\mathbf{x}, t_n; t)$ is the position at time t of the fluid particle (moving with velocity $\mathbf{u}(\mathbf{x}, t)$) which reaches the spatial point $\mathbf{x}$ at time t_n. Thus, the partial differential equation in (2) can be rewritten as:

$$\frac{\partial c_h(\mathbf{X}(\mathbf{x}, t_n; t), t)}{\partial t} = F\left(\mathbf{c}_h\left(\mathbf{X}\left(\mathbf{x}, t_n; t\right), t\right), t\right) \quad \text{in} \quad \Omega \times (t_{n-1}, t_n], \tag{4}$$

where we note that the discrete numerical solution $c_h(\mathbf{x}, t_n)$ of (2) at time t_n is equal to the numerical solution $c_h(\mathbf{X}(\mathbf{x}, t_n; t_n), t_n)$ of (4) since, by definition, $\mathbf{X}(\mathbf{x}, t_n; t_n) = \mathbf{x}$. Following (4), the numerical calculation of $c_h(\mathbf{x}, t_n)$ at instant t_n involves two stages: the first one, or Lagrangian stage, computes the initial solution $c_h^{n-1}(\mathbf{X}(\mathbf{x}, t_n; t_{n-1}))$ belonging to the finite element space V_h^n; the second one, or Eulerian stage, integrates a coupled reaction-diffusion problem along the characteristic curves, whose solution is to be found also in V_h^n.

A major advantage of semi-Lagrangian schemes is their ability to decouple the Navier-Stokes equations from the energy and species mass conservation equations, translating the former into a Stokes problem and the latter into purely parabolic equations [31], the particulars of which are to be discussed below.

2.1. The Lagrangian stage: computation of $\bar{c}_h(\mathbf{x}, t_{n-1})$

Two main difficulties arise in the calculation of $c_h^{n-1}(\mathbf{X}(\mathbf{x}, t_n; t_{n-1}))$: first, how to compute the departure points of the characteristic curves $\mathbf{X}(\mathbf{x}_i, t_n; t_{n-1})$ (or $\mathbf{X}^{n-1}(\mathbf{x}_i)$ in abbreviated form), for general points $\mathbf{x}_i$ in the triangulation; second, and most important, how to build, in the finite element space V_h^n in which we search for a solution of (4), the best approximation $\bar{c}_h^{n-1}(\mathbf{x}) = \bar{c}_h(\mathbf{x}, t_{n-1}) \in V_h^n$ to the actual function $c_h^{n-1}(\mathbf{X}(\mathbf{x}, t_n; t_{n-1}))$, since the latter does not belong to V_h^n.

An approach to the first problem would be to compute numerically the characteristic curves of a given point $\mathbf{x}_i$ by means, for instance, of an explicit, second-order Runge-Kutta scheme:

$$\begin{cases} \dfrac{d\mathbf{X}(\mathbf{x}_i, t_n; t)}{dt} = \mathbf{u}_h\left(\mathbf{X}(\mathbf{x}_i, t_n; t), t\right), & t_{n-1} \le t < t_n; \\ \mathbf{X}(\mathbf{x}_i, t_n; t_n) = \mathbf{x}_i; \end{cases} \tag{5}$$

where an explicit, linear (extrapolation) approximation to $\mathbf{u}_h(\mathbf{x}, t)$ is constructed using the previously computed velocities $\mathbf{u}_h^{n-1}(\mathbf{x}) \in V_h^{n-1}$ and $\mathbf{u}_h^{n-2}(\mathbf{x}) \in V_h^{n-2}$ at times t_{n-1} and t_{n-2}, respectively:

$$\mathbf{u}_h(\mathbf{x}, t) = \mathbf{u}_h^{n-1}(\mathbf{x}) + \left[\mathbf{u}_h^{n-1}(\mathbf{x}) - \mathbf{u}_h^{n-2}(\mathbf{x})\right] \frac{t - t_{n-1}}{\Delta t} + \mathcal{O}(\Delta t^2), \quad t_{n-1} \le t < t_n; \tag{6}$$

this provides a consistent second-order accuracy for the calculation of $\mathbf{X}(\mathbf{x}_i, t_n; t_{n-1})$, as shown in [33].

Once the departure points of the characteristic curves are known, it is possible to build $\bar{c}_h^{n-1}(\mathbf{x})$ as a good approximation to the actual function $c_h^{n-1}(\mathbf{X}(\mathbf{x}, t_n; t_{n-1}))$ in the current finite element space V_h^n; to this end, we write $\bar{c}_h^{n-1}(\mathbf{x}) \in V_h^n$ as a linear combination of the functions $\{\varphi_i^n\}$ forming a basis of the finite element space V_h^n, according to:

$$\bar{c}_h^{n-1}(\mathbf{x}) = \sum_{i=1}^{N_h^n} \overline{C}_i^{n-1} \varphi_i^n(\mathbf{x}), \tag{7}$$

where $\overline{C}_i^{n-1}$ is the set of unknown, nodal values of $\mathbb{T}_h^n$ to be determined.

5

As previously discussed, there are different approaches to build this approximation in a finite element framework: the classical semi-Lagrangian method [33] computes the departure points $\mathbf{X}(\mathbf{x}_i, t_n; t_{n-1})$ for the nodal mesh points $\mathbf{x}_i$ of the current triangulation by interpolation; in contrast, the Lagrange-Galerkin method [35] uses an L^2-projection scheme that, as will be shown below, produces better results than the classical interpolatory formulation. A variant of the Lagrange-Galerkin scheme, termed "semi-Lagrange-Galerkin" [37], has proved to be as accurate, and more efficient in terms of CPU time, than the pure Lagrange-Galerkin method. Below we give a brief description of both schemes, exploring afterwards the applicability of the semi-Lagrange-Galerkin technique in an anisotropic adaptive framework.

2.1.1. Classical semi-Lagrangian method

This method computes the value of $\overline{C}_i^{n-1} = \bar{c}_h^{n-1}(\mathbf{x}_i)$ via a standard Lagrange interpolation with polynomials of degree m, equal to the order of the finite element space V_h^n, for all nodal points $\{\mathbf{x}_i\}_{i=1}^{N_h^n}$ of the current mesh $\mathbb{T}_h^n$. We start by computing the characteristic curves $\mathbf{X}^{n-1}(\mathbf{x}_i)$ associated with the nodal points $\mathbf{x}_i$; since the function $c_h^{n-1}(\mathbf{x})$ belongs to V_h^{n-1}, we have to find the mesh element $K_{\mathbf{X}_i} \in \mathbb{T}_h^{n-1}$ in which the departure point $\mathbf{X}^{n-1}(\mathbf{x}_i)$ is located, via the search-locate algorithm presented in [45]. After that, we select the values $\left\{ C_{N_1}^{n-1}, C_{N_2}^{n-1}, \ldots, C_{N_{nv}}^{n-1} \right\}$ of the nv mesh nodal points of $K_{\mathbf{X}_i} \in \mathbb{T}_h^{n-1}$ which surround the departure point $\mathbf{X}^{n-1}(\mathbf{x}_i)$, noting that $nv = (m+1)(m+2)/2$ for triangles, and $nv = (m+1)(m+2)(m+3)/6$ for tetrahedra. Finally, the value of $\overline{C}_i^{n-1}$ is computed by interpolation with polynomials of degree m as:

$$\overline{C}_i^{n-1} = c_h^{n-1}\left(\mathbf{X}^{n-1}(\mathbf{x}_i)\right) = \sum_{j=1}^{N_h^{n-1}} C_j^{n-1} \varphi_j^{n-1}\left(\mathbf{X}^{n-1}(\mathbf{x}_i)\right), \tag{8}$$

where $\{\varphi_j^{n-1}\}_{j=1}^{N_h^{n-1}}$ is the set of basis functions of V_h^{n-1} defined for the triangulation $\mathbb{T}_h^{n-1}$ at the previous instant of time t_{n-1}.

2.1.2. Semi-Lagrange-Galerkin method

The next scheme considered is the semi-Lagrange-Galerkin method, in which the set of values $\{\overline{C}_i^{n-1}\}$ is obtained minimizing the following error in the L^2-norm:

$$\min \left\{ \int_\Omega \left[c_h^{n-1}\left(\mathbf{X}(\mathbf{x}, t_n; t_{n-1})\right) - \bar{c}_h^{n-1}(\mathbf{x}) \right]^2 d\Omega \right\}. \tag{9}$$

The solution to this minimization problem is the Galerkin L^2-projection of $c_h^{n-1}\left(\mathbf{X}^{n-1}(\mathbf{x})\right)$ onto the finite element space V_h^n, which is obtained solving the following systems of linear equations:

$$\sum_{i=1}^{N_h^n} m_{ji} \overline{C}_i^{n-1} = \int_\Omega c_h^{n-1}\left(\mathbf{X}^{n-1}(\mathbf{x})\right) \varphi_j^n(\mathbf{x}) \, d\Omega; \tag{10}$$

where $m_{ij} = \int_\Omega \varphi_i^n(\mathbf{x})\varphi_j^n(\mathbf{x}) \, d\Omega$ are the components of the mass matrix of the finite element space V_h^n. To compute the integral in the right-hand side of (10), we consider the contribution of each triangle belonging to the current triangulation $K \in \mathbb{T}_h^n$ and then we make use of quadrature rules. As it is, $\varphi_j^n(\mathbf{x})$ can be easily evaluated at the quadrature points $\mathbf{x}_g$ of K, via a linear mapping $\mathbf{x}_g = F_K^n(\widehat{\mathbf{x}}_g)$ between the reference triangle $\widehat{K}$ and the current triangle K. However, according to the Lagrange-Galerkin formulation of [35], it would be necessary to compute the feet of the characteristic curves for all quadrature points $\mathbf{X}^{n-1}(\mathbf{x}_g)$ of element K in order to evaluate $c_h^n\left(\mathbf{X}^{n-1}(\mathbf{x_g})\right)$, a process that is computationally expensive.

As an alternative, we propose here to use the cheaper semi-Lagrange-Galerkin method, which approximately computes $\mathbf{X}^{n-1}(\mathbf{x}_g)$ without loss of accuracy in the discretization. We define an isoparametric transformation $\widetilde{F}_K^{n*}$ from the reference element $\widehat{K}$ onto the transported

m-triangle $\widetilde{K}^*$ whose nodes are the nv feet of the characteristic curves of the nodes of element K $\left\{\mathbf{X}^{n-1}(\mathbf{x}_i)\right\}_{i=1}^{nv}$, so that $\mathbf{X}^{n-1}(\mathbf{x}_g)$ is approximated by $\widetilde{\mathbf{x}}_g^*$ according to:

$$\mathbf{X}^{n-1}(\mathbf{x}_g) \simeq \overline{\mathbf{x}}_g^* = \widetilde{F}_K^{n*}(\hat{\mathbf{x}}_g) = \sum_{i=1}^{n_v} \mathbf{X}^{n-1}(\mathbf{x}_i)\hat{\varphi}_i(\hat{\mathbf{x}}_g), \tag{11}$$

where $\{\hat{\varphi}_i\}_{i=1}^{nv}$ is the set of basis functions of the reference triangle $\widehat{K}$; see Fig. 1 for details.
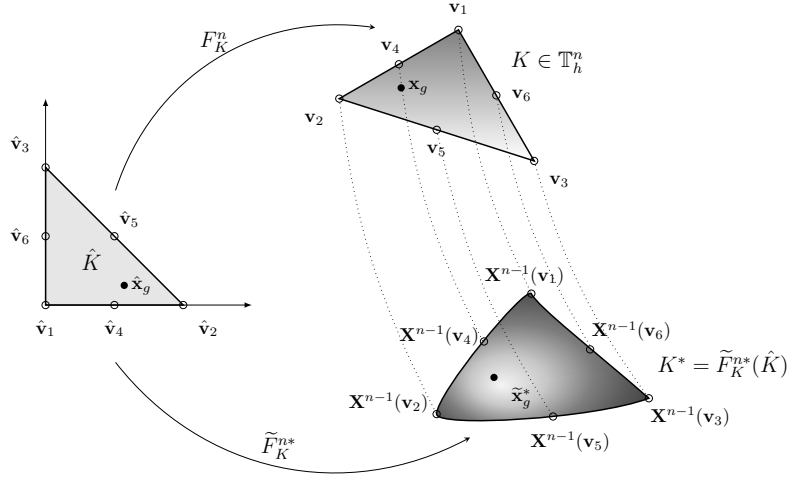
Figure 1: Representation of the mapping $F_K^n : \widehat{K} \to K$ and the isoparametric transformation $\widetilde{F}_K^{n*} : \widehat{K} \to \widetilde{K}^*$ adopted in the the semi-Lagrange-Galerkin method for quadratic finite elements $m = 2$.

The transformation $\widetilde{F}_K^{n*}$ of (11) has order m, the same order of the finite element space V_h^n where the solution of the problem is computed. Therefore, this approximation $\mathbf{X}^{n-1}(\mathbf{x}_g) = \widetilde{\mathbf{x}}_g^* + \mathcal{O}\left(h^{m+1}\right)$ provides an error that is consistent with the space discretization. In addition, to generate the isoparametric transformation $\widetilde{F}_K^{n*}$ for all elements K we just need to compute the characteristic curves for all nodal points $\{\mathbf{x}_i\}_{i=1}^{N_h^n}$ of the current mesh $\mathbb{T}_h^n$, the same requirement found in the classical semi-Lagrangian methodology. Hence, the proposed procedure just entails the resolution of a positive definite system of linear equations with a well-conditioned mass matrix, a very cheap procedure from a computational point of view. For reference purposes, in the numerical experiments presented below we use $NPG = 16$ Gaussian quadrature points for 2D configurations.

2.2. The Eulerian stage: computation of $c_h(\mathbf{x}, t_n)$

After the Lagrangian stage, one must find the solution of the partial differential equation (4) in the finite element space V_h^n. Let $\overline{c}_h(\mathbf{x}, t) \in V_h^n$ be the numerical solution of the problem:

$$\begin{cases} \dfrac{\partial \overline{c}_h(\mathbf{x}, t)}{\partial t} = F\left(\overline{\mathbf{c}}_h(\mathbf{x}, t), t\right) & \text{in} \quad \Omega \times (t_{n-1}, t_n], \\ \overline{c}_h^{n-1}(\mathbf{x}) = P_h^n\left(c_h^{n-1}(\mathbf{X}(\mathbf{x}, t_n; t_{n-1}))\right) & \text{in} \quad \Omega, \\ B\overline{c}_h^n(\mathbf{x})|_{\partial\Omega} = 0, \end{cases} \tag{12}$$

representing our approximation to the actual function $c_h(\mathbf{x}, t)$ of the generic problem (2) at time t_n, with $\overline{c}_h(\mathbf{x}, t_n) = c_h(\mathbf{x}, t_n)$. In this problem, $P_h^n\left(c_h^{n-1}(\mathbf{X}(\mathbf{x}, t_n; t_{n-1}))\right)$ denotes the interpolation (classical semi-Lagrangian) or projection (semi-Lagrange-Galerkin) operator over V_h^n employed in the Lagrangian stage.

7

For the spatial discretization of (12), we use a Galerkin finite element formulation along with a second order temporal scheme $\mathcal{O}\left(\Delta t^2\right)$ to be consistent with the computation of the characteristic curves for the convection operator discussed above. Below, we particularize (2) to the conservation equations involved in all combustion problems (1): energy, species mass fractions, and Navier-Stokes equations.

2.2.1. Temporal discretization of the energy and species mass conservation equations

One way of attacking the systems arising from the energy and species mass conservation equations would be to use an implicit BDF (Backward Differentiation Formula) of second order, thus benefiting from the unconditional stability of such schemes to take large time steps in the integration process. However, there is a major drawback to this approach, namely that for realistic combustion models, both the diffusion and reaction terms of (1) depend on the local thermodynamic state of the mixture, and they do so in a non-linear way. To make this point clear, let us remember that the unknown variables of the energy and species mass conservation equations are the $I-1$ species mass fractions plus a single state variable (usually the temperature), that we may collect in the vector-valued variable $\mathbf{c}_h(\mathbf{x}, t) = \{Y_{1h}, \ldots, Y_{(I-1)h}, T_h\}$ composed of I scalar variables. Thus, we may write I diffusion-reaction differential equations of the form:

$$\frac{\partial \bar{\mathbf{c}}_h(\mathbf{x}, t)}{\partial t} = \mathbf{F}\left(\bar{\mathbf{c}}_h(\mathbf{x}, t), t\right) \quad \text{in} \quad \Omega \times (t_{n-1}, t_n], \tag{13}$$

where the right-hand side $\mathbf{F}\left(\bar{\mathbf{c}}_h(\mathbf{x}, t), t\right)$ is a generic vector-valued function that may depend on the set of variables $\mathbf{c}_h$ in a highly nonlinear way due to the variation of the molecular transport coefficients with temperature and, particularly, to the strong temperature dependence of the chemical reaction rates. Therefore, an implicit discretization of the above system of equations (13) would eventually lead to a fully-coupled, non-linear system of equations that involves all the thermodynamic variables, so that, e.g., a Newton iteration should be employed to linearize the problem, often resulting in poorly conditioned matrices that require computationally expensive solvers. On the other hand, an explicit discretization of such terms avoids the coupled non-linear equations. However, the extreme stiffness of the reaction terms, which are often strongly dependent on temperature, poses a stability limit to the size of the time step Δt (according to the Courant-Friedrich-Levy (CFL) criterion), which may completely destroy the efficiency of such schemes.

To overcome the drawbacks of both methodologies, we propose to use an explicit method that improves the stability region of the temporal scheme by adding stages in a dynamic way. This temporal scheme takes the name of Runge-Kutta-Chebyshev scheme, and was developed initially for pure parabolic equations [46]. A version of that algorithm was first introduced in a local isotropic adaptive framework by Bermejo and Carpio [31] to solve convection-diffusion-reaction equations using classical semi-Lagrangian schemes. The algorithm proposed in this work consists of a second-order explicit Runge-Kutta-Chebyshev scheme (EX-RKC) with a variable number of stages r that depends on the stiffness of the system, so that it can be adaptively changed in time as the solution to the combustion problem evolves. The two first stages of the scheme are used to achieve second-order convergence in time, whereas additional stages are employed to increase the region of absolute stability. In this type of schemes, the stability region is a narrow strip along the negative real axis of the complex plane, with the real stability boundary being proportional to r^2; this quadratic dependency is derived from the Chebyshev polynomial of the first kind. Correspondingly, the number of stages r is defined in terms of the spectral radius $\rho(J_{\mathbf{F}})$ of the Jacobian matrix $J_{\mathbf{F}}$ built from the right-hand side term $\mathbf{F}(\bar{\mathbf{c}}_h^{n-1}(\mathbf{x}), t_{n-1}) = \{F_1(\bar{\mathbf{c}}_h^{n-1}, t_{n-1}), F_2(\bar{\mathbf{c}}_h^{n-1}, t_{n-1}), \ldots, F_I(\bar{\mathbf{c}}_h^{n-1}, t_{n-1})\}$ of (12), that is:

$$r = 1 + \text{Int}\left[\sqrt{1 + \Delta t \frac{\rho(J_{\mathbf{F}})}{0.653}}\right], \tag{14}$$

where Int[ ] is the integer part operator.

The spectral radius $\rho(J_{\mathbf{F}})$ takes into account the diffusion and reaction terms embedded in the right-hand side $\mathbf{F}(\mathbf{c}, t)$. At first sight, it would seem that the most relevant contribution to $\rho(J_{\mathbf{F}})$ would be that of the reaction terms; however, the local refinement of the highly-stiff reaction zones tends to balance out both contributions. For systems in which the number of stages is kept below a maximum, $r \leq r_{\max}$ (e.g., $r_{\max} \approx 100$ for typical combustion problems), the EX-RKC scheme is very efficient; exceeding the maximum number of stages would mean that highly non-linear chemical reactions are taking place at the flame and, appropriately, smaller elements are being produced by the adaptive procedure. This could be interpreted as an indication of the inability of the method to solve in an effective way the system of equations with the current time step size Δt; that would mean Δt is mainly ruled by the diffusive-reactive step more than by the convective step. Consequently, and although not considered in this work, an adaptation procedure for the time step Δt could be devised by ensuring that, at all times, the algorithm does not go beyond a fixed maximum number of stages $r_{\max}$. The EX-RKC scheme is detailed in [46], and it is also outlined here for completeness.

The calculation of the numerical solution $\mathbf{c}_h^n(\mathbf{x}) \in (V_h^n)^I = \overbrace{V_h^n \times \ldots \times V_h^n}^{I}$ of (12) by an EX-RKC scheme with r stages using at initial condition $\bar{\mathbf{c}}_h^{n-1}(\mathbf{x}) \in (V_h^n)^I$ for all $i = 1, \ldots, I$ may be written as:

$$
\begin{cases}
\mathbf{W}_h^0 = \bar{\mathbf{c}}_h^{n-1}(\mathbf{x}), \\
\mathbf{W}_h^1 = \mathbf{W}_h^0 + \widetilde{\mu}_1 \Delta t \mathbf{F}^0, \\
\textbf{for } j = 2 \textbf{ to } r \\
\quad \mathbf{W}_h^j = (1 - \mu_j - \nu_j)\mathbf{W}_h^0 + \mu_j \mathbf{W}_h^{j-1} + \nu_j \mathbf{W}_h^{j-2} + \quad \widetilde{\mu}_j \Delta t \mathbf{F}^{j-1} + \widetilde{\gamma}_j \Delta t \mathbf{F}^0, \\
\textbf{end} \\
\mathbf{c}_h^n(\mathbf{x}) = \mathbf{W}_h^r,
\end{cases}
\tag{15}
$$

where $\mathbf{W}_h^0, \ldots, \mathbf{W}_h^r$ are internal scalar variables belonging to $(V_h^n)^I$, and $\mathbf{F}^k = \mathbf{F}(\mathbf{W}_h^k, t_{n-1} + \alpha_k \Delta t)$. Besides, the coefficients appearing in (15) are given analytically by:

$$
\begin{cases}
\epsilon = \dfrac{2}{13}, \quad w_0 = 1 + \dfrac{\varepsilon}{r^2}, \quad w_1 = \dfrac{T_r'(w_0)}{T_r''(w_0)}, \\[2mm]
b_j = \dfrac{T_j''(w_0)}{\left(T_j'(w_0)\right)^2} \quad (2 \leq j \leq r), \quad b_0 = b_1 = b_2, \quad a_j = 1 - b_j T_j(w_0), \\[2mm]
\widetilde{\mu}_1 = b_1 w_1, \quad \mu_j = \dfrac{2 b_j w_0}{b_{j-1}}, \quad \nu_j = -\dfrac{b_j}{b_{j-2}}, \quad \widetilde{\mu}_j = \dfrac{2 b_j w_1}{b_{j-1}}, \quad \widetilde{\gamma}_j = -a_{j-1}\widetilde{\mu}_j, \\[2mm]
\alpha_j = w_1 \dfrac{T_j''(w_0)}{T_j'(w_0)} \quad (2 \leq j \leq r), \quad \alpha_1 = \dfrac{\alpha_2}{T_2'(w_0)} = \dfrac{\alpha_2}{4 w_0}, \quad \alpha_0 = 0
\end{cases}
\tag{16}
$$

with $T_j(x)$ the Chebyshev polynomial of the first kind and degree j. Finally, we obtain the numerical solution $\mathbf{c}_h^n(\mathbf{x}) \in (V_h^n)^I$ for quadratic ($m = 2$) finite elements for all the thermodynamic variables (temperature and species mass fractions). To do that, we derive the weak formulation of the equations (15), which eventually leads to an uncoupled, well-conditioned linear system of equations, one for each variable and for each of the stages of the scheme. We also note that the EX-RKC method was extended to advection-diffusion-reaction problems in [47]; such algorithm is also adequate for a purely Eulerian description of the flow using a stabilized, finite element formulation instead of the mixed Lagrangian-Eulerian scheme proposed in this work.

2.2.2. Temporal discretization of the Navier-Stokes equations

If one considers the flow of a viscous fluid with variable density at the low-Mach number limit, the governing Navier-Stokes equations can be written in the general form (12) as follows:

$$\rho \frac{\partial \bar{\mathbf{u}}_h(\mathbf{x},t)}{\partial t} = -\nabla \bar{p}_h(\mathbf{x},t) + \nabla \cdot \left\{ \mu \left[\nabla \bar{\mathbf{u}}_h(\mathbf{x},t) + \nabla \bar{\mathbf{u}}_h^T(\mathbf{x},t) \right] \right\} \quad \text{in} \quad \Omega \times (t_{n-1}, t_n], \qquad (17)$$

while also satisfying the continuity equation:

$$\frac{\partial \rho}{\partial t} + \mathbf{u}_h \cdot \nabla \rho = -\rho \nabla \cdot \mathbf{u}_h, \quad \text{or} \quad \nabla \cdot \mathbf{u}_h = -\frac{1}{\rho} \left(\frac{\partial \rho}{\partial t} + \mathbf{u}_h \nabla \rho \right) = -\frac{1}{\rho} \frac{D\rho}{Dt} = -\frac{D\log(\rho)}{Dt}. \quad (18)$$

From (17), the only unknowns are the velocity $\bar{\mathbf{u}}_h(\mathbf{x},t)$ and the (hydrodynamic) pressure $\bar{p}_h(\mathbf{x},t)$; the fluid properties ρ and μ are available since they are functions of the thermodynamic state of the mixture given by the integration of the above energy and species mass conservation equations at time t_n. We now use the second-order accurate BDF formula to discretize (17)-(18) in time [38], resulting in the following Stokes problem:

$$\begin{cases} \rho^n \dfrac{3\bar{\mathbf{u}}_h^n(\mathbf{x}) - 4\bar{\mathbf{u}}_h^{n-1}(\mathbf{x}) + \bar{\mathbf{u}}_h^{n-2}(\mathbf{x})}{2\Delta t} = -\nabla p_h^n(\mathbf{x}) + \nabla \cdot \left\{ \mu^n \left[\nabla \mathbf{u}_h^n(\mathbf{x}) + \nabla \mathbf{u}_h^{nT}(\mathbf{x}) \right] \right\}, \\ \nabla \cdot \mathbf{u}_h^n = -\left. \dfrac{D\log(\rho)}{Dt} \right|_{t_n}, \end{cases} \qquad (19)$$

with $\bar{\mathbf{u}}_h^{n-2}(\mathbf{x})$ calculated from $\mathbf{u}_h^{n-2}(\mathbf{X}(\mathbf{x},t_n;t_{n-2}))$ using the same algorithm employed for $\bar{\mathbf{u}}_h^{n-1}(\mathbf{x})$.

Our Galerkin discretization of the Stokes problem (19) uses Taylor-Hood finite elements, quadratric $m=2$ for the velocity and linear $m=1$ for the pressure, to satisfy the Ladyzenskaja-Babuska-Brezzi condition. Finally, the linear systems of equations arising from the spatial discretization are solved by a preconditioned conjugate gradient Uzawa algorithm developed by Dean and Glowinski [48].

2.3. Local anisotropic refinement algorithm

As already discussed, the large disparity of scales that characterizes practical combustion problems makes imperative the use of an efficient, adaptive, numerical method to properly capture the inner structure of the reacting mixing layers (in non-premixed systems) or the time evolution of the flame fronts (in premixed, or partially premixed, combustion). Here, we outline the anisotropic mesh refinement algorithm developed in [34], to exploit the strongly directional features exhibited by chemically reacting flows at moderately high Reynolds numbers. Accordingly, we refer the reader to that paper for details concerning the a priori and a posteriori error analysis. The key idea is to adapt the computational domain to the particularities of the solution at each time step. For that purpose, we first compute the numerical solution of our combustion problem; then, we evaluate a certain indicator of the error incurred by the spatial discretization; finally, we build an optimal mesh with the smallest possible number of elements that still satisfies a given tolerance for the error indicator $\eta^n \leq Tol$. An all-important component of the adaptation process is the so-called metric tensor, and entity which, by itself, contains the information required to define the shape, size and orientation of each mesh element in the "optimal" triangulation. Although there are several strategies to define such tensor based on some error indicators (see for example [49], [50]), in this work we follow the guidelines presented in [34] for convection dominated equations using semi-Lagrangian schemes.

Since combustion problems are typically multivariable process, the definition of the metric tensor proposed in [34] must be carried out separately for each scalar variable, taking then the intersection of all the resulting metric tensors. To this end, we define a set of variables

$$\phi = \{\beta_1 c_1(\mathbf{x},t), \dots, \beta_i c_i(\mathbf{x},t), \dots, \beta_N c_N(\mathbf{x},t)\} \qquad (20)$$

which will allow us to refine the mesh, where ϕ is a N selection of the unknown variables of our problem $\{T, Y_1, \ldots, Y_{I-1}, u_1, \ldots, u_d\}$. Moreover, α_i is a normalizing constant associated with the variable $c_i(\mathbf{x}, t)$ to balance the contribution of each variable in the global error. We define the global error in the L^2-norm at the final instant of time t_f as:

$$e_{L^2}^2(t_f) = \sum_{i=1}^{N} \beta_i^2 e_{L^2}^2(c_{if}) \quad \text{with} \quad e_{L^2}(c_{if}) = \|c_i(t_f) - c_{ih}(t_f)\|_{L^2(\Omega)} \quad \forall c_i \in \phi. \tag{21}$$

Typically, $\beta_i = \langle \max_{\mathbf{x}} \{c_{ih}(\mathbf{x}, t)\}\rangle_t^{-1}$, that is, the inverse of the mean value in time of the maximum value in space for each variable, though the actual values must be defined for each problem (see Sections 3.1 and 3.2 for two illustrative examples).

Consequently, the metric tensor defined for each variable is given by:

$$M_K^i = |K^i|^{-2/d} R_K^i \left(S_K^i\right)^{-1} \left(R_K^i\right)^T, \tag{22}$$

where the matrix $R_K^i = \{\mathbf{r}_{1,K}^i, \ldots, \mathbf{r}_{d,K}^i\}$ with $\mathbf{r}_{n,K}^i \cdot \mathbf{r}_{m,K}^i = \delta_{nm}$ (the Kronecker delta), the stretching factors matrix $S_K^i = \text{diag}\{s_{1,K}^i, \ldots, s_{d,K}^i\}$ and the scalar $|K^i|$ define, respectively, the orientation, the shape and the size of the optimal (triangular, $d = 2$, or tetrahedral, $d = 3$) element associated with the variable $c_{ih}^n(\mathbf{x})$ at time t_n. To calculate this set of parameters according to [34], we need to define for each variable $c_{ih}^n(\mathbf{x})$, its Hessian matrix tensor $H_{iK}(c_{ih}^n)$ as well as an a posteriori error indicator η_{iK}^n for each element in the current triangulation $K \in \mathbb{T}_h^n$. The evaluation of the Hessian matrix can be carried out using the numerical solution $c_{ih}^n(\mathbf{x})$ and taking the weak formulation of each of the derivatives appearing in $H_K(c_{ih}^n(\mathbf{x}))$, as explained in [51]. As a posteriori error indicator we evaluate the local or truncated error in the L^2-norm between $c_{ih}^{n-1}(\mathbf{X}^{n-1}(\mathbf{x}))$ and $\bar{c}_{ih}^{n-1}(\mathbf{x})$. This is the error incurred in the Lagrangian stage or, equivalently, the error incurred by the information transfer process when moving from one mesh $\mathbb{T}_h^{n-1}$ to the next triangulation $\mathbb{T}_h^n$:

$$\eta_{iK}^n = \beta_i \left(\int_K \left[c_{ih}^{n-1}(\mathbf{X}^{n-1}(\mathbf{x})) - \bar{c}_{ih}^{n-1}(\mathbf{x}) \right]^2 d\Omega \right)^{1/2}, \tag{23}$$

whereas the total error is computed as:

$$\eta^n = \left(\sum_{i=1}^{N} (\eta_i^n)^2 \right)^{1/2} \quad \text{with} \quad \eta_i^n = \left(\sum_{K \in \mathbb{T}_h^n} (\eta_{iK}^n)^2 \right)^{1/2}. \tag{24}$$

A linear analysis, presented in [34], shows that the optimal orientation and shape of the element K can be computed from the eigenvector-eigenvalue pair $\{\mathbf{l}_{i,K}, g_{i,K}\}$ of the Hessian matrix $H_{iK}(c_{ih}^n)$ as:

$$s_{j,K}^i = \left(\prod_{j=1}^{d} |g_{j,K}| \right)^{1/d} \left| g_{d+1-j,K}^{-1} \right|, \quad \mathbf{r}_{j,K}^i = \mathbf{l}_{d+1-j,K}, \quad \text{for} \quad j = 1, \ldots, d. \tag{25}$$

It is important to note that the previous result was derived in a linear finite element framework; however, in convection dominated combustion problems we usually observe strongly anisotropic features with exponential behaviour, such as reacting mixing layers or premixed flame fronts, and the shape and the orientation derived from the Hessian works quite well independently of the order of the finite element space. Let us also point out that higher-order finite elements in anisotropic mesh adaptation is still a topic of intensive research, pioneered by Houston and coworkers for unstructured triangular meshes [52–54]. From the a posteriori error indicator η_{iK}^n of (23), we can compute the new size of the element $|K^i|$ so as to have as few elements as possible, while still satisfying $\eta_i^n = (\sum_{K \in \mathbb{T}_h^n} (\eta_{iK}^n)^2)^{1/2} \leq Tol/N$. From [34]:

$$|K^i| = |K| \left(\frac{(Tol/N)^2}{\sum_{K \in \mathbb{T}_h^n} (\eta_{iK}^n)^{2/(2\alpha+1)}} \right)^{1/(2\alpha)} (\eta_{iK}^n)^{-2/(2\alpha+1)}, \tag{26}$$

with $|K|$ the current size of the element and $\alpha = (m+1)/d$ (m the order of the finite element space).

Next, we define a metric intersection procedure to deal with the set of metrics $\{M_K^1, \ldots, M_K^N\}$ defined in (22) for the set of variables ϕ of (20), in order to obtain a single metric at a given element $K \in \mathbb{T}_h^n$. Following [51] along with [50], we state the following

Proposition 1. *If A and B are two metric tensors, its intersection is formed by the eigenvectors $P = \{P_1, \ldots, P_d\}$ of the matrix $A^{-1}B$ which simultaneously diagonalizes both quadratics forms: $\mathrm{diag}\{a_1, \ldots, a_d\} = P^T A P$ and $\mathrm{diag}\{b_1, \ldots, b_d\} = P^T B P$. Hence, the intersection of A and B is $A \cap B = P\,\mathrm{diag}\{\max(a_1, b_1), \ldots, \max(a_d, b_d)\}P^T$.*

For more than two metrics, the problem is harder to deal with, since the intersection operator is not commutative. In this paper, we proceed in an iterative way, first applying the intersection operator to a pair of metrics, and subsequently intersecting the result of the previous step with the next metric. The final metric, M_K^{opt}, is then normalized with the minimum value of the optimal size of the current element across all metrics, that is, $\min(|K^1|, |K^2|, \ldots, |K^N|)$, such that

$$\det\left|M_K^{\mathrm{opt}}\right| = \min\left(|K^1|, |K^2|, \ldots, |K^N|\right)^{-1}. \tag{27}$$

Note that, for isotropic adaptation, the metric is given by the identity tensor normalized in a similar manner. Finally, the metric tensor is passed on to an anisotropic mesh generator, such as BAMG [55] for 2D triangular meshes. For reference purposes, the local adaptive anisotropic procedure for combustion problems described in this section is summarized in Algorithm 1.

Algorithm 1: Local adaptive anisotropic algorithm for combustion problems.

Data: Combustion equations (1) with initial condition $\mathbf{c}^0(\mathbf{x}) = \{T^0, Y_1^0, \ldots, Y_{I-1}^0, \mathbf{u}^0\}$; spatial domain Ω; temporal domain $[0, t_f]$; time step size Δt and spatial tolerance Tol.

Result: Numerical solution $\mathbf{c}_h^n(\mathbf{x}) = \{T_h^n, Y_{1h}^n, \ldots, Y_{(I-1)h}^n, \mathbf{u}_h^n\} \in (V_h^n)^{I+d}$.

1 **compute** $\mathbf{c}_h^0(\mathbf{x})$ from $\mathbf{c}^0(\mathbf{x})$ by Galerkin L^2-projection and define $\mathbb{T}_h^0$, so that $\eta^0 < Tol$.

2 **set** $\mathbb{T}_h^1 = \mathbb{T}_h^0$, $t_1 = \Delta t$.

3 **while** $t_n \leq T$ **do**

4   **repeat**

5   **apply** Lagrangian stage: **compute** $\bar{\mathbf{c}}_h^{n-1}(\mathbf{x}) \in (V_h^n)^{I+d}$ by classical semi-Lagrangian scheme (8) or semi-Lagrange-Galerkin scheme (10).

6   **apply** Eulerian stage: **compute** solution $\mathbf{c}_h^n(\mathbf{x})$ on current triangulation $\mathbb{T}_h^n$.

    • **solve** diffusion-reaction equations for the temperature and species mass fraction variables $\{Y_{1h}^n, \ldots, Y_{(I-1)h}^n, T_h^n\}$ via an EX-RKC scheme (15).

    • **solve** Stokes problem (19) to obtain the velocity $\mathbf{u}_h^n$ at time t_n.

7   **compute** metric tensor M_K^{opt} to make local anisotropic adaptation.

    • **compute** Hessian and spatial local error indicator η_i^n by means of (23) for each variable $i = 1, 2, \ldots, N$ defined in ϕ (20).

    • **compute** Metric tensor M_K^i for each variable $i = 1, 2, \ldots, N$ (22).

    • **compute** intersection of elemental metrics $M_K^{\mathrm{opt}} = M_K^1 \bigcap \cdots \bigcap M_K^N$ with Proposition 1 and (27).

8   **compute** optimal triangulation $\mathbb{T}_h^{\mathrm{opt}}$ from optimal metric M_K^{opt} with BAMG [55].

9   **set** $\mathbb{T}_h^n = \mathbb{T}_h^{\mathrm{opt}}$ as triangulation for next iteration.

10   **until** ($\eta^n \leq Tol$);

11   **set** $\mathbb{T}_h^{n+1} = \mathbb{T}_h^{\mathrm{opt}}$, and $t_{n+1} = t_n + \Delta t$.

12 **end**

---

3. Numerical examples: Flame/vortex interaction

Although several approaches have been employed for the simulation of low Mach number reacting flows, a well-established benchmark configuration for the analysis and validation of time-dependent numerical codes still does not exist [12]. Unlike other fields (e.g., compressible flow) where the governing equations are crystal clear, in the combustion community there is not a common approach regarding the modeling of molecular transport and chemical reaction terms, which has precluded the establishment of such a benchmark problem. As a result, we decided to tackle one canonical example that has been extensively studied both experimentally and numerically over the years: the interaction of a flame with a vortex. From the physical point of view, the flame/vortex interaction constitutes a well-defined system of intermediate complexity between steady laminar flames and turbulent flames, which offers fundamental understanding of processes involving the coupling between fluid dynamics and combustion. From the mathematical point of view, the capturing of a very thin flame sheet evolving in time due to the interaction with a vortex is a useful benchmark configuration to evaluate the efficiency of any time-dependent numerical method in an anisotropic adaptive framework. Moreover, we shall consider the two kind of flames found in combustion devices: premixed and non-premixed (i.e., diffusion) flames.

The first test (Test I) corresponds to a planar 2D configuration featuring the interaction of a vortex pair with a laminar premixed flame, described with simplified transport and chemistry descriptions; this problem has been studied by many authors (see for instance [8, 10, 39, 40] and references therein). The purpose here is to compare our numerical results with those of the references, showing the enhanced accuracy of the semi-Lagrange-Galerkin scheme (using an L^2-projection) compared with the classical semi-Lagrangian scheme (which employs interpolation). Further, with this model we thoroughly assess the performance and convergence rate of the proposed adaptive numerical algorithm, for uniform, isotropic and anisotropic meshes.

The second test (Test II) corresponds to a 2D-axisymmetric configuration featuring the head-on interaction of a laminar vortex ring with a counterflow diffusion flame established between two opposed streams of fuel and air. This configuration has captured the interest of experimental and numerical researchers alike [12, 41–44]. In that problem, we present a moderately complex model for the description of nitrogen-diluted hydrogen-air non-premixed flame/vortex interactions which, in addition to the analysis of the numerical features of the proposed algorithm, allows us to perform a qualitatively comparison with experimental visualizations found in the literature.

### 3.1. Test I: Planar premixed flame/vortex interaction

In this test, we study the time evolution of a laminar premixed flame that is perturbed by a vortex pair in a planar 2D configuration. We consider that the flame is initially located at the middle of the computational domain, separating a fresh reactive mixture at room temperature and pressure from a burnt mixture of combustion products at the adiabatic flame temperature. The fresh mixture is perturbed by two counter-rotating vortices that interact head-on with the flame, causing its elongation and distortion due to the local strain induced by the vortices. For this test, we take as main reference the work by Lessani et al. [10], using the same combustion model and fluid properties.

3.1.1. Test I: Governing equations

For a firmer grasp of the physical processes involved in the flame/vortex interaction, the conservation equations must be written in non-dimensional form; in what follows, primes are used to denote dimensional quantities, while non-primed quantities are dimensionless. We consider as reference values the fluid properties ρ_0', μ_0', c_{p0}', D_{T0}' evaluated at the fresh mixture. For the sake of simplicity, the reactive mixture is assumed to be diluted in inert gases (as for the example the Nitrogen of the air), meaning that the mixture molecular weight and transport

properties are those of the inert species. Then, the dimensionless mixture molecular weight and specific heat at constant pressure can be assumed to be constant: $W = 1$, and $c_p = 1$. As reference velocity we use the propagation velocity of the planar premixed flame u'_0, and as reference length we take the characteristic flame thickness $L'_0 = D'_{T0}/u'_0$.

The chemical model consists of a simple one-step overall reaction

$$R \text{ (reactants)} \rightarrow P \text{ (products)} + (Q) \text{ (heat)}$$
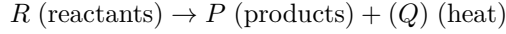
with Arrhenius kinetics, which in dimensionless form can be written as:

$$\dot{m}_R = \frac{L'_0}{u'_0} B' \rho Y_R \exp(-T_a/T), \tag{28}$$

where T_a is the dimensionless activation temperature, B' is the pre-exponential factor and Y_R is the normalized reactant mass fraction (unity in the fresh mixture and zero in the burnt gases).

The assumption that the inert species are dominant implies that Fick's law can be used to define the species mass diffusion flux; further assuming that the diffusivity of the reactants is equal to the thermal diffusivity (unity Lewis number), we can write the non-dimensional diffusion flux as:

$$\mathbf{j}_R = -\rho D_T \nabla Y_R.$$

With all these considerations, the general conservation equations combustion problems at low Mach number (1) can be written for Test I in the non-dimensional form:

$$\begin{cases} \dfrac{\partial \rho}{\partial t} + \nabla \cdot (\rho \mathbf{u}) = 0, \\[2mm] \rho \left(\dfrac{\partial \mathbf{u}}{\partial t} + \mathbf{u} \cdot \nabla \mathbf{u} \right) = -\nabla p + \dfrac{Pr_0}{Pe_0} \nabla \cdot \left\{ \mu \left[\nabla \mathbf{u} + (\nabla \mathbf{u})^T \right] \right\}, \\[2mm] \rho \left(\dfrac{\partial Y_R}{\partial t} + \mathbf{u} \nabla Y_R \right) = \dfrac{1}{Pe_0} \nabla \cdot (\rho D_T \nabla Y_R) - \dot{m}_R, \\[2mm] \rho \left(\dfrac{\partial T}{\partial t} + \mathbf{u} \nabla T \right) = \dfrac{1}{Pe_0} \nabla \cdot (\rho D_T \nabla T) + \Delta h_R^0 \dot{m}_R, \end{cases} \tag{29}$$

where Δh_R^0 denotes the non-dimensional heat release per unit mass of reactant, with the adiabatic temperature given by $T_f = 1 + \Delta h_R^0$, and

$$Pe_0 = \frac{u'_0 L'_0}{D'_{T0}} \quad \text{and} \quad Pr_0 = \frac{\mu'_0}{\rho'_0 D'_{T0}},$$

are the Peclet and Prandtl numbers, respectively.

For the system of equations (29) to be consistent, we must add an state equations for ρ and two constitutive relations for μ and ρD_T in terms of the unknowns of the problem. On the one hand, we assume that the mixture is a perfect gas, so that for a constant molecular weight and at the low Mach number limit, ρ depends only on temperature. On the other hand, a simplified power law is used to define the dynamic viscosity and thermal diffusivity. Hence, we have:

$$\rho = \frac{1}{T} \quad \text{and} \quad \mu = \rho D_T = T^{0.7}.$$

Following Lessani et al. [10], in the numerical study to be presented below we have chosen the model parameters so as to approximate those of the stoichiometric methane/air flame at normal conditions: $u'_0 = 0.416 \, \text{m s}^{-1}$, $L'_0 = D'_{T0}/u'_0 = 5.45 \times 10^{-5} \, \text{m}$, $T_a = 30$, $B' = 7 \times 10^6 \, \text{s}^{-1}$, and $\Delta h_R^0 = 6.4$ (hence $T_f = 7.4$). With this choice of parameters, both the Peclet and the Prandtl number take values very close to unity, i.e., $Pe_0 = 1.0$ and $\text{Pr}_0 = 0.7$.

Boundary conditions. For the numerical solution of Test I we use a rectangular domain in the (x, y) plane of size $[0, 100] \times [0, 200]$. At the bottom of the domain, we impose inflow boundary conditions with the variables taking the reference values of the fresh mixture, namely $T = 1$, $Y_R = 1$, and $\mathbf{u} = (u_x, u_y) = (0, 1)$. At the top of the domain, we impose outflow boundary conditions, with null momentum, heat, and mass diffusion fluxes. Finally, at the lateral walls we impose null heat and mass diffusion fluxes, along with a free-slip boundary condition for the velocity.

at $y = 0$	at $y = 200$	at $x = 0$ and $x = 100$
$(u_x, u_y) = (0, 1)$,	$\left(-p + \dfrac{Pr_0}{Pe_0}\mu\left[\nabla\mathbf{u} + (\nabla\mathbf{u})^T\right]\right) \cdot \mathbf{e}_y = \mathbf{0}$,	$u_x = 0$,
$Y_R = 1$,	$\partial Y_R/\partial y = 0$,	$\partial Y_R/\partial x = 0$,
$T = 1$.	$\partial T/\partial y = 0$.	$\partial T/\partial x = 0$.

$$\tag{30}$$

Initial condition. For the temporal integration, we take a time interval from $t = 0$ to $t_f = 25$. To define the initial condition, we consider the steady, one-dimensional, laminar premixed flame located in the middle of the domain at $y = 100$ along the x direction. We find the steady solution (denoted by a subscript s) by integrating the conservation equations (29) until the final steady state is reached, using the boundary conditions (30) along with an initial profile for all the variables involved consisting of two different uniform states. One way to check the validity of the solution is to verify that it satisfies the following relations between the variables of the steady, one-dimensional, premixed flame [7]: $u_{ys}(y) = T_s(y)$ (a first integral of the continuity equation yields $\rho_s u_{ys} = 1$), and $T_s(y) = 1 + \Delta h_R^0(1 - Y_{Rs}(y))$. Moreover, since the problem is translation-invariant, we include as additional condition so that at $y = 100$ the mass fraction of the reactant takes the value $Y_{Rs} = 0.78$, as in [10]. As a result, the initial condition is determined by $T(\mathbf{x}, 0) = T_s$, $Y_R(\mathbf{x}, 0) = Y_{Rs}$, with the velocity consisting of the superposition of the initial steady velocity $(u_{xs}, u_{ys}) = (0, T_s)$ with the velocity field generated by two linear vortices, one rotating in the counterclockwise sense located at $(x_1, y_1) = (37.5, 75)$ and the other rotating clockwise at $(x_2, y_2) = (62.5, 75)$. Hence,

$$\mathbf{u}(\mathbf{x}, 0) = \begin{cases} u_x = -\dfrac{\Gamma}{R^2}\left[e^{-r_1^2/2}(y - y_1) - e^{-r_2^2/2}(y - y_2)\right], \\ u_y = T_s + \dfrac{\Gamma}{R^2}\left[e^{-r_1^2/2}(x - x_1) - e^{-r_2^2/2}(x - x_2)\right], \end{cases}$$

where $\Gamma = 70$ represents the dimensionless vortex strength, $R = 4$ is the dimensionless vortex radius, and $r_i = \sqrt{(x - x_i)^2 + (y - y_i)^2}$ measures the local distance to the core of vortex i.

3.1.2. Test I: Numerical results

The numerical solution for Test I is retrieved using a small time step size $\Delta t = 5 \cdot 10^{-3}$ so as to make time discretization errors negligible. For the mesh adaptation procedure, we take a tolerance Tol to create a metric tensor using the set of variables

$$\phi = \{Y_R, T/7, u_x/10, u_y/10\} \tag{31}$$

according to section 2.3. Then, in order to evaluate the performance and capabilities of the numerical algorithm, we compute the solution using first a uniform mesh and then isotropic and anisotropically adapted meshes, employing both the classical semi-Lagrangian scheme and the new semi-Lagrange-Galerkin algorithm.

First, we compare the results of our simulation with those by Lessani et al. [10]. To that end, we consider the numerical solution obtained using the proposed local anisotropic adaptive algorithm and the semi-Lagrange-Galerkin scheme, with a tolerance $Tol = 4 \cdot 10^{-2}$. In Figure

15

2 we show the evolution of the distorted premixed flame through the isolines of temperature at different instants of time. To highlight the adaptation process, and taking advantage of the symmetry of the simulation, the left panel in each subplot displays the adaptive mesh, whereas the right panel shows isolines of vorticity. This Figure compares very favorably with Figure 12 of reference [10]. Initially the vortices are far from the flame front, which remains virtually unperturbed, but as they come closer the flame starts to be significantly stretched and distorted, eventually developing a cusp-like shape at later times.
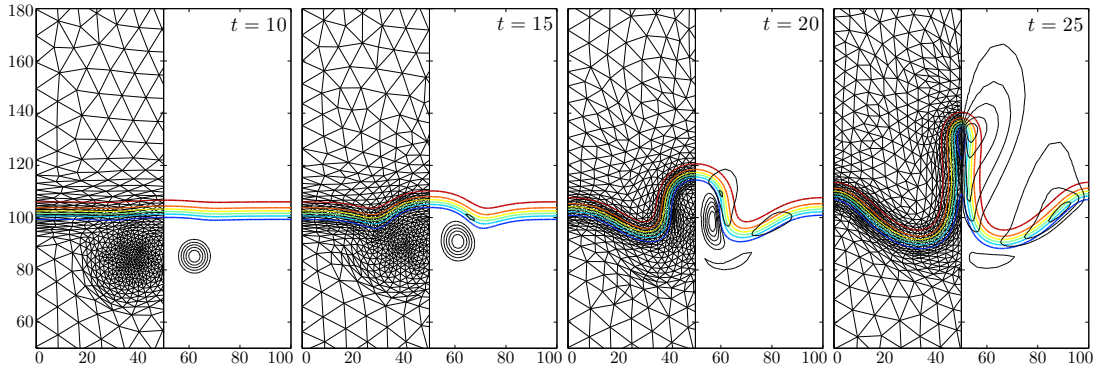
Figure 2: Isolines of temperature and vorticity for Test I. In the left panel of the figures we can see a detail of the adapted anisotropic meshes.

Figure 3 shows profiles of density, $\rho = 1/T$, reactant mass fraction, Y_R, and y-velocity component, u_y, along the centerline at time $t = 25$. As can be seen, our results are in excellent agreement with those Lessani et al. [10], which have also been plotted for comparative purposes; in that work, the most refined mesh consisted of 262144 elements. In contrast, here we just need tolerances $Tol \leq 4 \cdot 10^{-2}$ to achieve convergence, producing meshes with an average number of elements $\overline{NE} < 2500$. In particular, the time evolution of the number of elements NE_n is shown in Figure 4 for four different tolerances: the number of elements is maximum at the start of the simulation, which coincides with the maximum strength of the vortices at $t = 0$; after that, the vortices grow weaker as fluid viscosity takes on, and the number of elements required to achieve the same degree of accuracy decreases. At time $t \simeq 12.5$ the vortices start their interactions with the flame and the number of elements grows again.

Next, we investigate the performance of the proposed algorithm and its convergence rate. First, we focus on the spatial capabilities of the adaptive procedure, comparing the solution provided by a fixed, uniform mesh, with those obtained using isotropic and anisotropically
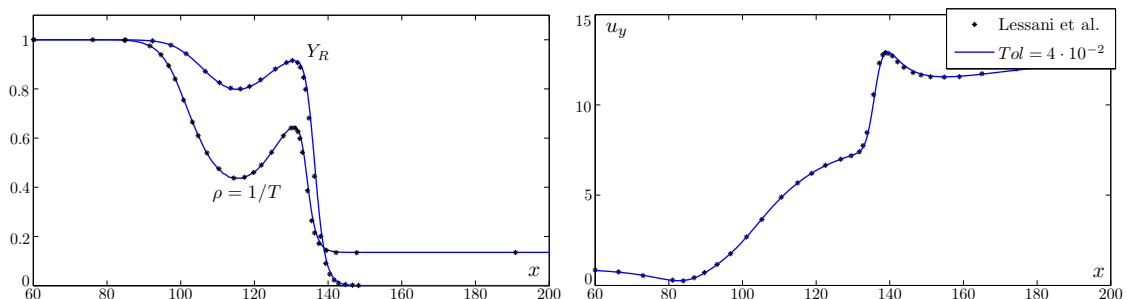
Figure 3: Profiles of density, $\rho = 1/T$, reactant mass fraction, Y_R, (left panel) and y-velocity component, u_y, (right panel) for Test I at $x = 50$ at time $t = 25$.

16
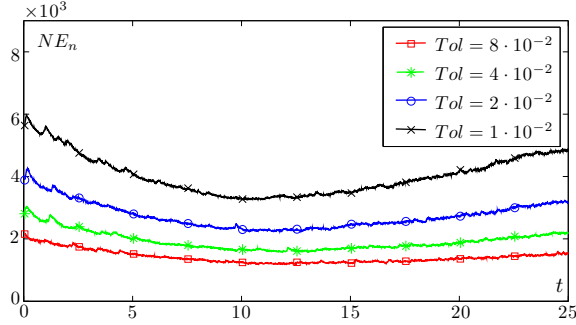
Figure 4: Evolution of the number of elements for the anisotropic adaptive algorithm NE_n for different tolerances in Test I.

adapted meshes. Second, we show the enhanced accuracy of the semi-Lagrange-Galerkin scheme (with L^2-projection) compared with the classical semi-Lagrangian scheme (which uses interpolation). Thus, we start by measuring the global error at the end of the numerical integration ($t = t_f$) in the L^2-norm $e_{L^2}(t_f)$ for the set of variables defined in (31), using the definition of (21):

$$e_{L^2}(t_f) = \left\{ \frac{1}{49} e_{L^2}^2(T_f) + e_{L^2}^2(Y_{Rf}) + \frac{1}{100} e_{L^2}^2(u_{xf}) + \frac{1}{100} e_{L^2}^2(u_{yf}) \right\}^{1/2}. \tag{32}$$

This global error is computed considering as the "exact" (i.e., reference) solution a numerical solution computed with the small time step size $\Delta t = 5 \cdot 10^{-3}$ and a very small tolerance $Tol = 1 \cdot 10^{-3}$, using the more accurate semi-Lagrange-Galerkin scheme in an anisotropic adaptation procedure. The results are collected in Table 1, where for each numerical simulation, we have included its tolerance, the average number of elements $\overline{NE}$ and the global error $e_{L^2}(t_f)$.

Table 1: Average number of elements $\overline{NE}$ and global L^2-error $e_{L^2}(t_f)$ for different numerical simulations of Test I.

Semi-Lagrangian (SL) scheme

Anisotropic adapted mesh			Isotropic adapted mesh			Uniform fixed mesh	
Tol	$\overline{NE}$	$e_{L^2}(t_f)$	Tol	$\overline{NE}$	$e_{L^2}(t_f)$	$\overline{NE}$	$e_{L^2}(t_f)$
$2 \cdot 10^{-2}$	$2.94 \cdot 10^3$	4.456	$2 \cdot 10^{-2}$	$3.05 \cdot 10^3$	1.840	$4.20 \cdot 10^3$	11.91
$1 \cdot 10^{-2}$	$4.25 \cdot 10^3$	2.246	$1 \cdot 10^{-2}$	$4.50 \cdot 10^3$	0.845	$9.18 \cdot 10^3$	5.215
$5 \cdot 10^{-3}$	$6.32 \cdot 10^3$	0.993	$5 \cdot 10^{-3}$	$6.96 \cdot 10^3$	0.435	$2.04 \cdot 10^4$	0.990
$2 \cdot 10^{-3}$	$1.11 \cdot 10^4$	0.351	$2 \cdot 10^{-3}$	$1.26 \cdot 10^4$	0.238	$4.54 \cdot 10^4$	0.402

Semi-Lagrangian-Galerkin (SLG) scheme

Anisotropic adapted mesh			Isotropic adapted mesh			Uniform fixed mesh	
Tol	$\overline{NE}$	$e_{L^2}(t_f)$	Tol	$\overline{NE}$	$e_{L^2}(t_f)$	$\overline{NE}$	$e_{L^2}(t_f)$
$8 \cdot 10^{-2}$	$1.42 \cdot 10^3$	0.276	$8 \cdot 10^{-2}$	$1.38 \cdot 10^3$	0.491	$4.20 \cdot 10^3$	7.845
$4 \cdot 10^{-2}$	$1.93 \cdot 10^3$	0.090	$4 \cdot 10^{-2}$	$1.94 \cdot 10^3$	0.241	$9.18 \cdot 10^3$	1.611
$2 \cdot 10^{-2}$	$2.74 \cdot 10^3$	0.045	$2 \cdot 10^{-2}$	$2.82 \cdot 10^3$	0.088	$2.04 \cdot 10^4$	0.496
$1 \cdot 10^{-2}$	$4.04 \cdot 10^3$	0.021	$1 \cdot 10^{-2}$	$4.32 \cdot 10^3$	0.027	$4.54 \cdot 10^4$	0.081

From Table 1, we may state the following properties concerning the classical semi-Lagrangian (SL) and the semi-Lagrange-Galerkin (SLG) schemes: for a uniform mesh, the SLG scheme shows better accuracy than the SL method, but only by a factor of two; if we focus our attention on isotropic refinement for both SL and SLG schemes, one notices that, for the same degree of

17

mesh refinement, attained using approximately the same tolerance (e.g. $Tol = 2 \cdot 10^{-2}$ and $Tol = 1 \cdot 10^{-2}$), the SLG scheme is roughly 30 times as accurate as the LG method, whereas for anisotropic refinement the increased accuracy offered by the SLG technique achieves a factor of order 100; further, we observe how the adaptive procedure and the resulting metric tensor are *efficient* in the sense that, when the spatial tolerance is halved, the global error is divided approximately by a factor of 2; finally, a global comparison of the adaptive mesh refinement techniques shows that the anisotropic method is roughly twice as accurate as the isotropic procedure when the SLG scheme is used, and provides much better accuracy ($\sim 400\times$) than a uniform mesh. However, for the classical SL scheme the advantages are not as sharply defined: indeed, anisotropic adaptation improves the accuracy obtained using a uniform mesh, but it seems to achieve a slightly lower accuracy when compared with isotropic adaptation. After an in-depth study of this phenomenon, we lean towards the hypothesis that the culprit is the highly diffusive character of the SL scheme when applied to the computation of the velocity field; this, along with adaptive refinement techniques and frequently changing meshes, transfers the numerical error of solving the Navier-Stokes equations to the remaining conservation equations, thus damaging the overall accuracy of the method.

We may alternatively arrive at the same conclusions by inspecting Figure 5, where we plot the average number of elements $\overline{NE}$ against the global error $e_{L^2}(t_f)$; as a consequence, we can compute the convergence rate of the global error with the average number of elements $e_{L^2}(t_f) \propto \overline{NE}^{-\alpha}$. The theoretical L^2-error given by the a priori error analysis for smooth solutions is $\alpha = (m+1)/d$, $(d = 2, 3)$; in our case with $d = 2$ and quadratic finite elements $m = 2$, $\alpha = 1.5$. The estimated convergence rate $\widehat{\alpha}$ using linear regression is also displayed in Figure 5. As can be observed, the SLG scheme using the projection technique gives much lower errors than the classical approach, as well as a better convergence rate (superconvergence effect $\widehat{\alpha} \sim 2.5$). Further, we notice the advantages of using anisotropic adaptation instead of a fixed, uniform mesh. However, the benefits of anisotropic versus isotropic refinement are not as clear-cut in this example, due to the lack of strong anisotropic features of the flow (there is no dramatic stretching of the flame produced by the vortex, see Figure 2). To highlight the mildly anisotropic character of this test, let us note that the maximum streaching factor achieved throughout these simulations is $\max(s_K) \sim 8$. Accordingly, and to make clear the benefits of anisotropic mesh refinement, we study next a situation where the flame stretches to a much higher extent than in this reference case.
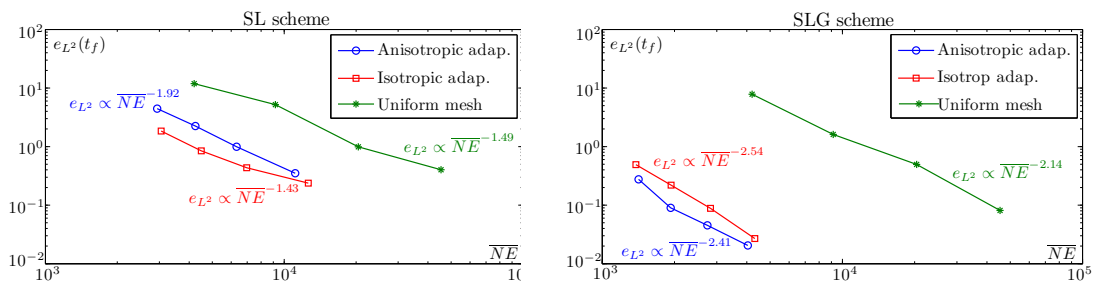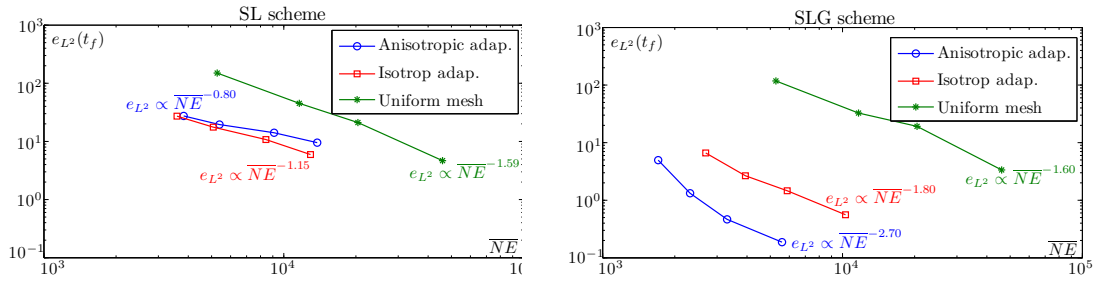

Figure 5: Convergence in the L^2-norm of the global error for Test I. Classical Semi-Lagrangian (SL) (left) and semi-Lagrange-Galerkin (SLG) (right) schemes for uniform, isotropic and anisotropic adapted meshes.

3.1.3. Test I: Numerical results with stronger anisotropy

The setup of this example is identical to that of Test I, with the same conservation equations (29), but now using a characteristic length $L_0' = 16.35 \cdot 10^{-5}$ m, three times larger than in the previous example. This translates into a threefold increase in the Peclet number, now $Pe_0 = 3$, and a more vigorous chemical reaction according to (28). The time step size is $\Delta t = 2 \cdot 10^{-3}$,

whereas the spatial tolerance varies in the range $Tol = [10, 5, 2, 1] \times 10^{-2}$ for the SL scheme, and $Tol = [20, 10, 5, 2] \times 10^{-2}$ for the SLG scheme; as the "exact" (i.e., reference) solution we consider a numerical solution computed with the same time step size and the smallest spatial tolerance $Tol = 2 \cdot 10^{-3}$ using the more accurate SLG scheme and anisotropic adaptation. Figure 6 shows the evolution of the flame front as it is crossed by the vortex. We notice a higher degree of anisotropy in the optimal mesh produced by the adaptive algorithm, with quite stretched elements in the regions close to the flame front. In this set of simulations the maximum streaching factor is $\max(s_K) \sim 30$. As Pe_0 rises, the intensity of the flame/vortex interaction becomes more evident, with the vortex producing a much larger distortion of the flame and its surroundings (e.g. Figure 6, third panel). The estimated convergence rates $\widehat{\alpha}$ obtained in this case are reported in Figure 7. The anisotropic results are almost an order of magnitude better than those provided by the isotropic refinement with the SLG scheme. However, as was also indicated in previous test, the results with the SL scheme for isotropic, anisotropic adaptation, and uniform mesh are quite similar.
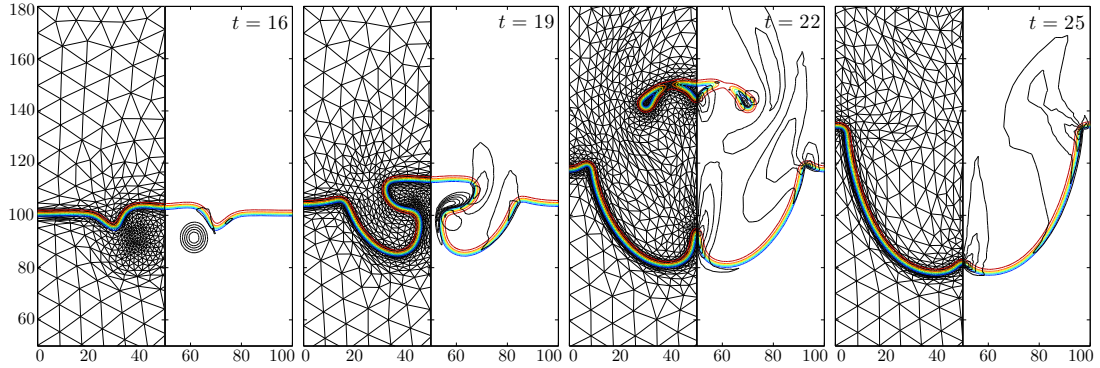
Figure 6: Isolines of temperature and vorticity for Test I with $Pe_0 = 3$. In the left panel of the figures we can see a detail of the adapted anisotropic meshes.

Figure 7: Convergence in the L^2-norm of the global error for Test I with $Pe_0 = 3$. Classical semi-Lagrangian (SL) (left) and semi-Lagrange-Galerkin (SLG) (right) schemes for uniform, isotropic and anisotropic adapted meshes.

As a summary of our simulations in Test I, we collect the most relevant parameters for $Pe_0 = 1$ and $Pe_0 = 3$ in Table 2, including the individual contributions to the global error $e_{L^2}(t_f)$ as defined in (32), using our anisotropic SLG scheme. We may observe the good behavior of the algorithm, with a balanced contribution of each of the variables to the global error.

Table 2: Results for $Pe_0 = 1$ and $Pe_0 = 3$ in Test I, using the local anisotropic SLG scheme. Mean number of elements $\overline{NE}$, global L^2-error $e_{L^2}(t_f)$, and individual contributions.

$Pe_0 = 1.0$, anisotropic SLG scheme in Test I

Tol	$\overline{NE}$	$e_{L^2}(t_f)$	$e_{L^2}(T_f)/7$	$e_{L^2}(Y_{Rf}))$	$e_{L^2}(u_{xf})/10$	$e_{L^2}(u_{yf})/10$
$8 \cdot 10^{-2}$	$1.42 \cdot 10^3$	0.276	0.1045	0.1143	0.0722	0.2166
$4 \cdot 10^{-2}$	$1.93 \cdot 10^3$	0.090	0.0389	0.0425	0.0289	0.0627
$2 \cdot 10^{-2}$	$2.74 \cdot 10^3$	0.045	0.0234	0.0255	0.0168	0.0235
$1 \cdot 10^{-2}$	$4.04 \cdot 10^3$	0.021	0.0083	0.0091	0.0063	0.0151

$Pe_0 = 3.0$, anisotropic SLG scheme in Test I

Tol	$\overline{NE}$	$e_{L^2}(t_f)$	$e_{L^2}(T_f)/7$	$e_{L^2}(Y_{Rf}))$	$e_{L^2}(u_{xf})/10$	$e_{L^2}(u_{yf})/10$
$20 \cdot 10^{-2}$	$1.70 \cdot 10^3$	4.974	2.5019	2.7203	1.5072	2.9675
$10 \cdot 10^{-2}$	$2.31 \cdot 10^3$	1.322	0.6152	0.6650	0.4193	0.8660
$5 \cdot 10^{-2}$	$3.30 \cdot 10^3$	0.466	0.2492	0.2712	0.1289	0.2539
$2 \cdot 10^{-2}$	$5.60 \cdot 10^3$	0.187	0.1084	0.1187	0.0498	0.0820

3.2. Test II: Axisymmetric non-premixed flame/vortex interaction

In many combustion devices, fuel and oxidizer enter the combustion chamber separately, so that the combustion process takes place in the form of non-premixed (or diffusion) flames [56]. In Test II, we explore the axisymmetric configuration where two coaxial counterflowing streams of fuel (hydrogen diluted with nitrogen, with mass fractions of fuel Y_{F0} and nitrogen $Y_{N_20} = 1 - Y_{F0}$) and air (with mass fractions of oxygen Y_{O_2A} and nitrogen $Y_{N_2A} = 1 - Y_{O_2A}$) simultaneously mix and react in a laminar mixing layer [41]. In particular, we analyze the perturbations introduced in the resulting counterflow diffusion flame by a coaxial vortex ring that is impulsively introduced in the computational domain moving head-on to the flame from the air side. As a result of the perturbation flow induced by the vortex, a large variety of interaction regimes may arise, including weakly distorted flames, strong flame wrinkling and roll-up, annular and axial extinction events followed by reignition via edge flames, as well as overall flame extinction [56]. In this test, we simulate several case studies presented by Renard et al. [57] with three main goals: to provide a moderately complex model for the description of nitrogen-diluted hydrogen-air diffusion flame/vortex interactions; to present a quantitative convergence study of the anisotropic adaptive, semi-Lagrange-Galerkin procedure; and lastly, to compare qualitatively our numerical results with experimental visualizations taken from the literature [57].

3.2.1. Test II: Governing equations

As in Test I, the conservation equations are also written in non-dimensional form using appropriate characteristic scales. The characteristic length is here the radius of the vortex ring r'_0 at the time it crosses the plane of the unperturbed mixing layer ($z = 0$). The characteristic time is the inverse of the strain rate A'^{-1}_A experienced by the flame prior to the interaction evaluated on the air side of the mixing layer. Additional reference values include the fluid properties of the air feed stream (denoted by a subscript A), defined at standard temperature $T'_0 = 300\,\text{K}$ and pressure $p'_0 = 1\,\text{atm}$ and assuming $Y_{O_2A} = 0.233$: density, ρ'_A, viscosity, μ'_A, thermal diffusivity, D'_{TA}, heat capacity, c'_{pA}, and molecular weight, W'_A. Again, all dimensional values have a prime. The solution to the problem is obtained by the integration of the low-Mach number Navier-Stokes equations, coupled with the energy and species mass conservation

equations:

$$\begin{cases} \dfrac{\partial \rho}{\partial t} + \nabla \cdot (\rho \mathbf{u}) = 0, \\[2mm] \rho \left(\dfrac{\partial \mathbf{u}}{\partial t} + \mathbf{u} \cdot \nabla \mathbf{u} \right) = -\nabla p + \dfrac{Pr_A}{Pe_0} \nabla \cdot \left\{ \mu \left[\nabla \mathbf{u} + (\nabla \mathbf{u})^T \right] \right\} \\[2mm] \rho c_p \left(\dfrac{\partial T}{\partial t} + \mathbf{u} \cdot \nabla T \right) = \dfrac{1}{Pe_0} \nabla \cdot (\rho D_T c_p \nabla T) - \mathcal{R} \displaystyle\sum_{i=1}^{I} h_i \dot{m}_i - \left(\displaystyle\sum_{i=1}^{I} \mathbf{j}_i c_{pi} \right) \cdot \nabla T, \\[2mm] \rho \left(\dfrac{\partial Y_i}{\partial t} + \mathbf{u} \cdot \nabla Y_i \right) = \dfrac{-1}{Pe_0} \nabla \cdot \mathbf{j}_i + \mathcal{R} \dot{m}_i \qquad \forall \, i = 1, \dots, I-1. \end{cases} \tag{33}$$

Using the previous characteristic scales, two dimensionless numbers arise naturally in the formulation of (33), namely the Peclet number of the unperturbed flow Pe_0, and the robustness of the flame $\mathcal{R}$, defined as follows:

$$Pe_0 = \frac{A'_A r'^2_0}{D'_{TA}}, \qquad \mathcal{R} = \frac{A'_e}{A'_A}. \tag{34}$$

The Peclet number Pe_0 measures the relative importance between convection and diffusion in the unperturbed mixing layer; alternatively, it can be written as the square of the ratio between the characteristic radius of the vortex ring r'_0, and the characteristic thickness of the unperturbed mixing layer, $\delta'_{m0} = (D'_{TA}/A'_A)^{1/2}$. The robustness of the flame $\mathcal{R}$ indicates how far from extinction is the flame at the initial, unperturbed condition [43]; it is defined in terms of A'_e, the critical strain rate at extinction of the unperturbed diffusion flame, which represents a characteristic chemical time that depends on the thermodynamic state of the feed streams (determined by the parameters T'_0, p'_0, Y_{F0}, and $Y_{O_2 A}$) and has to be obtained prior to starting the unsteady calculations. Another parameter that shows up in the equations is the Prandtl number of the air stream, $Pr_A = \mu'_A/(\rho'_A D'_{TA}) = 0.714$, which will be kept constant throughout this study.

The system of equations (33) must also be supplied with appropriate state equations and constitutive relations for the evaluation of the thermodynamic and transport properties of the fluid: the dimensionless density ρ, viscosity μ, heat capacity c_p, thermal diffusivity D_T, and, for the I chemical species of the mixture, the heat capacity c_{pi} and enthalpy h_i. Besides, we must specify the dimensionless species diffusion flux vector $\mathbf{j}_i$ for species i, as well as a suitable chemical kinetic model to evaluate the dimensionless chemical source terms $\dot{m}_i$.

State equations and constitutive relations. The dramatic increase in computing power over the last few decades has allowed the use of increasingly complex descriptions of molecular transport and chemical-kinetics in the numerical simulation of combustion problems. In the context of flame/vortex interactions, these modeling improvements, combined with state-of-the-art numerical methods, have enabled the detailed study of local flame extinction and re-ignition phenomena. However, since the characteristic scales associated with the chemistry are typically much smaller than the scales introduced by the vortex, these realistic models involve the integration of a set of highly-stiff partial differential equations, making their numerical solution much more expensive. In such a situation, the use of a method capable of solving efficiently and accurately the conservation equations, becomes critical. In return for those efforts, one may expect an improved predictive ability of the numerical model derived from a systematic comparison of the simulations with experimental data.

Following standard practice, the fluid is assumed to be a mixture of ideal gases, so that the density may be computed as

$$\rho = \frac{W}{T}, \tag{35}$$

where $W = (\sum_{i=1}^{I} Y_i/W_i)^{-1}$ is the dimensionless molecular weight of the mixture. We have neglected above the spatial variations experienced by the absolute pressure, which in the low-Mach number limit are small compared with the thermodynamic pressure, $p_0' = 1$ atm. The dynamic viscosity of the mixture μ, and the thermal conductivity of the mixture $\lambda = \rho D_T c_p$ are evaluated following a mixture average model as:

$$\mu = \frac{1}{2}\left(\sum_{i=1}^{I} X_i\mu_i + \frac{1}{\sum_{i=1}^{I} X_i/\mu_i}\right) \quad \text{and} \quad \lambda = \frac{1}{2}\left(\sum_{i=1}^{I} X_i\lambda_i + \frac{1}{\sum_{i=1}^{I} X_i/\lambda_i}\right),$$

where $X_i = (W/W_i)Y_i$ is the molar fraction of species i, and μ_i and λ_i are the dimensionless viscosity and thermal conductivity of species i.

The diffusion velocity of the chemical species is calculated using the generalized Fick's law

$$\mathbf{j}_i = \rho Y_i \mathbf{V}_{di}, \tag{36}$$

where the diffusion velocity consists of three contributions, $\mathbf{V}_{di} = \mathbf{V}_i^D + \mathbf{V}_i^T + \mathbf{V}_c$, namely the ordinary-diffusion velocity $\mathbf{V}_i^D$; the thermal-diffusion velocity $\mathbf{V}_i^T$ (responsible for the Soret effect); and the correction velocity $\mathbf{V}_c$, necessary to ensure that $\sum_{i=1}^{I} \mathbf{j}_i = \mathbf{0}$. The definition of these diffusion velocities is given by:

$$\mathbf{V}_i^D = -\frac{D_i}{X_i}\nabla X_i, \quad \mathbf{V}_i^T = \frac{D_i\theta_i}{X_i}\frac{\nabla T}{T}, \quad \text{and} \quad \mathbf{V}_c = -\sum_{i=1}^{I}\left(Y_i\mathbf{V}_i^D + Y_i\mathbf{V}_i^T\right), \tag{37}$$

where D_i is the diffusion mass coefficient, given explicitly in terms of the binary diffusion coefficients D_{ij} as:
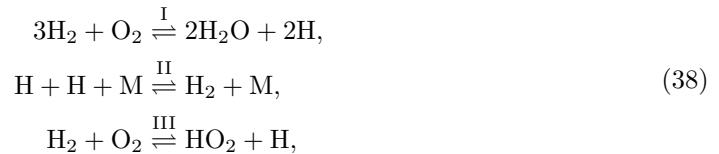
$$D_i = \frac{1 - Y_i}{\sum_{j=1,j\neq i}^{I} X_j/D_{ij}},$$

while θ_i represents the thermal-diffusion relation of species i in the mixture, negligible for all species except for the light ones, with values $\theta_{H_2} = 0.29$ and $\theta_H = 0.23$ [59]. The dimensionless variables μ_i, λ_i, and D_{ij} for the pure chemical species i are functions of the temperature, and are given by the expressions and data of the CHEMKIN library [60]. Moreover, the specific heat capacity of the mixture is computed from the heat capacity of the species i, by the expression

$$c_p = \sum_i^I c_{pi} Y_i,$$

where the dimensionless heat capacity c_{pi} and mass enthalpy h_i of species i (the latter also appearing in the general equations (33)) are functions exclusively of the temperature, and are computed using the NASA polynomials [61].

Regarding the chemical-kinetic model, a reduced mechanism suitable for the description of diluted non-premixed hydrogen-air combustion is considered [62]. In particular, we use a explicit, three-step reduced model proposed by Boivin et al. [63], which has been validated in different flame configurations and is known to describe with sufficient accuracy extinction strain rates in non-premixed counterflow flames. The three-step mechanism includes a branching reaction (I), a recombination reaction (II), and an initiation reaction (III):

$$3H_2 + O_2 \underset{}{\overset{I}{\rightleftharpoons}} 2H_2O + 2H,$$
$$H + H + M \underset{}{\overset{II}{\rightleftharpoons}} H_2 + M, \tag{38}$$
$$H_2 + O_2 \underset{}{\overset{III}{\rightleftharpoons}} HO_2 + H,$$

involving $I - 1 = 5$ reacting species, namely H_2, O_2, H, HO_2, and H_2O. This kinetic mechanism provides the dimensionless chemical source terms $\dot{m}_i$ appearing in the species conservation

equations:

$$
\begin{cases}
\dot{m}_{\mathrm{H_2}} = W'_{\mathrm{H_2}}(-3w'_{\mathrm{I}} + w'_{\mathrm{II}} - w'_{\mathrm{III}})/(\rho'_A A'_e), \\
\dot{m}'_{\mathrm{O_2}} = W'_{\mathrm{O_2}}(-w'_{\mathrm{I}} - w'_{\mathrm{III}})/(\rho'_A A'_e), \\
\dot{m}'_{\mathrm{H}} = W'_{\mathrm{H}}(2w'_{\mathrm{I}} - 2w'_{\mathrm{II}} + w'_{\mathrm{III}})/(\rho'_A A'_e), \\
\dot{m}'_{\mathrm{HO_2}} = W'_{\mathrm{HO_2}}w'_{\mathrm{III}}/(\rho'_A A'_e), \\
\dot{m}'_{\mathrm{H_2O}} = 2W'_{\mathrm{H_2O}}w'_{\mathrm{I}}/(\rho'_A A'_e),
\end{cases}
\tag{39}
$$

where the reaction rates w'_{I}, w'_{II} and w'_{III}, are computed in terms of the temperature and species mass fractions according to the guidelines provided in [63], with the reaction constants taken from the San Diego mechanism [64].

Boundary conditions. In our study, we assume an axisymmetric configuration with the positive z-axis pointing towards the fuel side. Thus, we choose as computational domain the cylinder defined by the dimensionless radial coordinates $0 \leq r \leq r_{\max}$, and the axial coordinates $z_{\min} < z < z_{\max}$. The air stream comes from $z = z_{\min}$ with oxygen mass fraction $Y_{\mathrm{O_2}A}$, while the fuel stream, diluted with nitrogen, comes from $z = z_{\max}$ with fuel mass fraction Y_{F0}. Both streams are at standards conditions of temperature $T = 1$. For the moderately large values of the Peclet number Pe_0 that are considered here, the mixing between both streams occurs only in a thin layer. Outside of this, the two coaxial counterflowing streams produce a nearly inviscid, axisymmetric, laminar stagnation-point flow with a known potential velocity field.

According to the above, we set Dirichlet boundary conditions at the top and bottom boundaries of our domain, as follows:

at $z = z_{\min}$	at $z = z_{\max}$
$(u_r, u_z) = (r/2, -z_{\min})$,	$(u_r, u_z) = (\rho_F)^{-1/2}(r/2, z_0 - z_{\max})$,
$Y_{O_2} = Y_{O_2 A}$, $Y_{N_2} = 1 - Y_{O_2 A}$,	$Y_F = Y_{F0}$, $Y_{N_2} = 1 - Y_{F0}$,
$Y_i = 0$, $\forall\, i \neq O_2, N_2$,	$Y_i = 0$, $\forall\, i \neq F, N_2$,
$T = 1$;	$T = 1$;

$$\tag{40}$$

where $\rho_F = W'_F/W'_A$ is the air to fuel density ratio; $z = 0$ represents the apparent location of the stagnation plane as seen from the air side, and z_0 is the apparent displacement of this plane as seen from the fuel side, due to the thermal expansion of the gases in the unperturbed flame. This displacement z_0 is of the order of the dimensionless thickness of the mixing layer $Pe_0^{-1/2}$, but its exact must be calculated as part of the unperturbed, steady solution of the vortex-free counterflow. On the other hand, the air and fuel streams are assumed to leave the computational domain through the lateral boundary, where we set the outflow boundary conditions given by the pressure distribution of the inviscid potential velocity field found in (40), along with the conditions of vanishing heat and mass diffusion fluxes for all chemical species. That is:

at $r = r_{\max}$

$$
\left(-p + \frac{Pr_A}{Pe_0}\mu\left[\nabla\mathbf{u} + \nabla\mathbf{u}^T\right]\right) \cdot \mathbf{n} =
\begin{cases}
\left(\dfrac{r_{\max}^2}{8} + \dfrac{(z - z_0)^2}{2}\right)\mathbf{n} & z_0 < z, \\[2mm]
\dfrac{r_{\max}^2}{8}\mathbf{n} & 0 < z < z_0, \\[2mm]
\left(\dfrac{r_{\max}^2}{8} + \dfrac{z^2}{2}\right)\mathbf{n} & z < 0,
\end{cases}
\tag{41}
$$
$$\nabla Y_i \cdot \mathbf{n} = 0, \quad \forall\, i,$$
$$\nabla T \cdot \mathbf{n} = 0,$$

where $\mathbf{n}$ denotes the unit normal vector pointing outwards from the computational domain.

Initial condition. As initial condition we consider the steady, unperturbed counterflow diffusion flame obtained from the numerical integration of (33), subject to the boundary conditions (40)–(41). This provides us with the steady velocity, $\mathbf{u}_s = (u_{rs}, u_{zs})$, temperature, T_s, and species mass fraction, Y_{is}, distributions. The iterative computation of the steady solution also yields the value of the apparent displacement z_0.

Once the steady solution has been computed, a coaxial vortex ring is introduced in the computational domain, moving head-on to the flame from the air side; its addition to the unperturbed straining field (u_{rs}, u_{zs}) provides the instantaneous velocity field (u_r, u_z):

$$
\mathbf{u}(\mathbf{x}, 0) = \begin{cases} u_r = u_{rs} + \dfrac{\tilde{\Gamma}}{\pi r_c} \left(\dfrac{r_c}{2r}\right)^{3/2} \left(\dfrac{z - z_c}{r_c}\right) I_1(\xi) \left[1 - e^{-(\varrho/\delta_v)^2}\right], \\[3mm] u_z = u_{zs} + \dfrac{\tilde{\Gamma}}{\pi r_c} \left(\dfrac{r_c}{2r}\right)^{3/2} \left[\dfrac{r}{r_c} I_1(\xi) - I_0(\xi)\right] \left[1 - e^{-(\varrho/\delta_v)^2}\right], \end{cases} \tag{42}
$$

where $\tilde{\Gamma}$ is the dimensionless vortex strength, which represents the ratio of the characteristic strain rate imposed by the vortex to the baseline strain rate:

$$
\tilde{\Gamma} = \frac{\Gamma'_0}{2r_0'^2} A'_A. \tag{43}
$$

In addition, $(r_c(t), z_c(t))$ denote the motion of the center of the vortex core, defined explicitly in [43, 58] as a function of time. This expression assumes that, at time $t = 0$, the vortex crosses the plane $z_c(0) = 0$, having a non-dimensional, unit size $r_c(0) = 1$. Note that the superposition of the baseline strain and the perturbation flow imposed by the vortex is only justified when both flows are irrotational, a condition which is satisfied far away from the variable density, mixing layer, prior to the interaction process. Accordingly, we take as the initial instant of time t_0 for our simulations the situation when $z_c(t_0) \simeq z_{\min}/2$. The remaining parameters appearing in (42) are the non-dimensional distance to the center of the vortex core $\varrho = [(r - r_c)^2 + (z - z_c)^2]^{1/2}$; the elliptic integrals $I_0(\xi)$ and $I_1(\xi)$ of argument $\xi = [(r - r_c)^2 + (z - z_c)^2]/(2rr_c)$; and the vorticity core radius $\delta_v = (8Pr_A/Pe_0)^{1/2}$.

3.2.2. Test II: Numerical examples

In this section we carry out a series of numerical experiments for various combinations of the dimensionless parameters Pe_0, $\mathcal{R}$, and $\tilde{\Gamma}$ defined in (34) and (43). In the laboratory, the flame position is usually determined by measuring the molar concentration of the hydroxyl radical OH; thus, Figures 8–10 depict the evolution of the diffusion flame by showing the computed isocontours of C_{OH}. The concentration C_{OH} can be easily obtained from the mass fractions of the reacting species H_2, O_2, H, HO_2, and H_2O by means of the algebraic relations given by Boivin et al. [63], derived from steady state assumptions applied for OH an other intermediate species. Further, the numerical integration of the combustion equations (33) is accomplished using the semi-Lagrange-Galerkin technique in an anisotropic adaptive framework. The integration domain is defined in a 2D axisymmetric configuration with $z_{\min} = -10$, $z_{\max} = 10$, $r_{\max} = 5$, and time $t \in [-0.4, 1.0]$; the time step size is $\Delta t = 10^{-3}$. In addition, for the mesh adaptation process we consider the set of variables

$$
\phi = \{\beta_T T, \beta_H Y_H, \beta_u u_r, \beta_u u_z\} \tag{44}
$$

according to section 2.3, where $\{\beta_T, \beta_H, \beta_u\}$ will be defined in each numerical experiment as the inverse of the characteristic value of each variable during the corresponding simulation.

Next, we explore three different instances of Pe_0, $\mathcal{R}$, and $\tilde{\Gamma}$, showing the results offered by our method with a fixed tolerance $Tol = 1 \cdot 10^{-2}$. After that, we study the evolution of the number of elements in an optimal mesh, for each of the three situations; finally, we compare the convergence rates achieved by our semi-Lagrange-Galerkin adaptation method.

24

Case 1: Weak flames. We start by examining the case of a weak flame characterized by a robustness $\mathcal{R} = 3$. The mass concentration of the fuel stream is $Y_{F0} = 0.015$, the Peclet number is $Pe_0 = 30$, and the strength of the vortex is given by $\tilde{\Gamma} = 30$. The parameters β_i used for the spatial adaptation are $\{\beta_T, \beta_H, \beta_u\} = \{4.5, 2 \times 10^{-4}, 30\}^{-1}$. Figure 8 shows our numerical results at different instants of time; we see how the diffusion flame undergoes axial extinction, producing a flame hole that recedes away from the axis and grows with time until the flame eventually disappears from the domain.
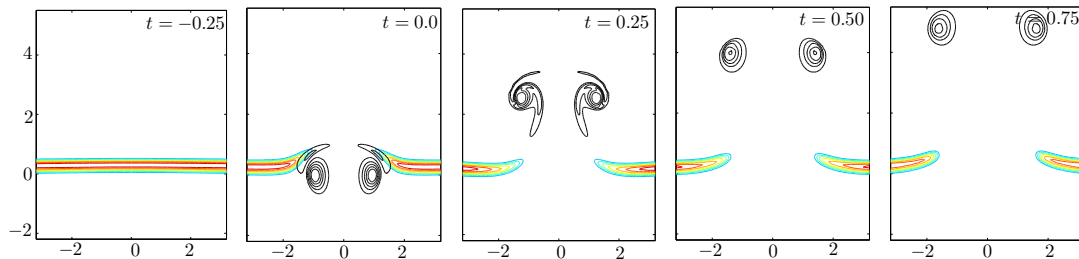
Figure 8: Numerical simulation of a weak flame with $Pe_0 = 30$, $\widetilde{\Gamma} = 30$ y $\mathcal{R} = 3$.

Case 2: Local extinction followed by reignition caused by active flame fronts. Here, we replicate the conditions of Case 1 studied by Renard et al. in [57]. The mass concentration for the fuel is $Y_{F0} = 0.015$, whereas the remaining dimensionless parameters defined by the experimental conditions are $Pe_0 = 25$, $\tilde{\Gamma} = 30$, and $\mathcal{R} = 20$. The parameters β_i used for the spatial adaptation are $\{\beta_T, \beta_H, \beta_u\} = \{5.5, 3 \times 10^{-4}, 10\}^{-1}$. As shown in Fig. 9, the vortex is now able to cause local flame extinction despite the large robustness of the flame. The remaining flame then travels up the stem pulled by the vortex, getting anchored in the fold that forms between the stem and the vortex, until it eventually reignites the unburned mixture pocket that travels with the vortex, thereby healing the flame. We also point out the noteworthy resemblance between our numerical results and the experimental visualizations shown in Fig. 10 of [57], which have been reproduced here for comparison purposes.
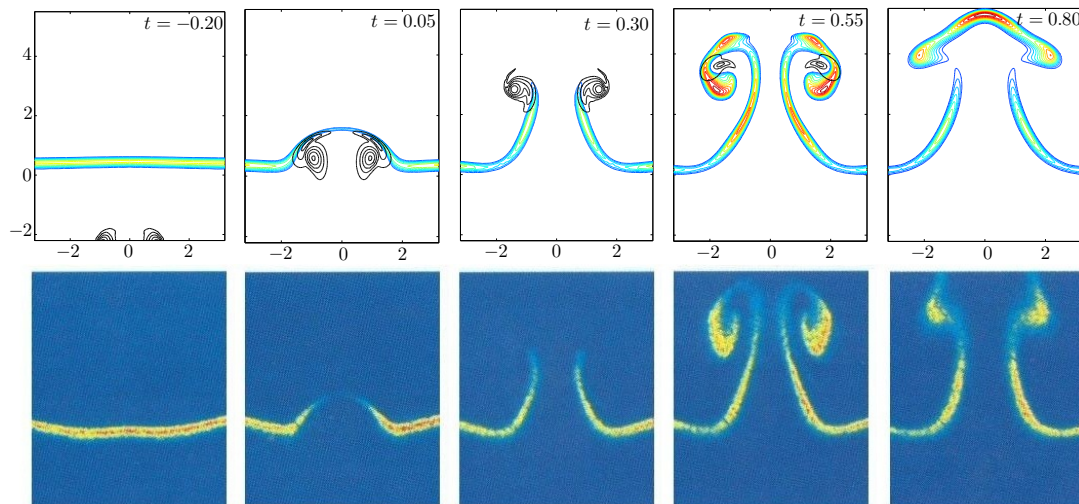
Figure 9: Top panel: numerical simulation of a local extinction of the flame and re-ignition with $Pe_0 = 25$, $\widetilde{\Gamma} = 30$ y $\mathcal{R} = 20$. Bottom panel: Fig. 10 of [57] (reprinted with permission from Elsevier). The numerical and experimental results are shown at exactly the same instants of time.

25

Case 3: Infinitely robust flames. Our last numerical experiment corresponds to Case 3 of [57]. In this situation $Y_{F0} = 0.029$, and the rest of the parameters governing the flow are $Pe_0 = 30$, $\tilde{\Gamma} = 40$, and $\mathcal{R} = 60$. The parameters β_i used for the spatial adaptation are $\{\beta_T, \beta_H, \beta_u\} = \{7, 4 \times 10^{-4}, 10\}^{-1}$. In Fig. 10 we compare our numerical solution with the experimental visualizations shown in Fig. 12 of [57], at the same instants of time. Again, we note the excellent agreement between the numerical results and the actual experiment. We can also observe how the infinite robustness of the flame prevents now its extinction, while the high temperatures experienced by the vortex during its interaction with the flame eventually causes it to disappear due to viscous dissipation.
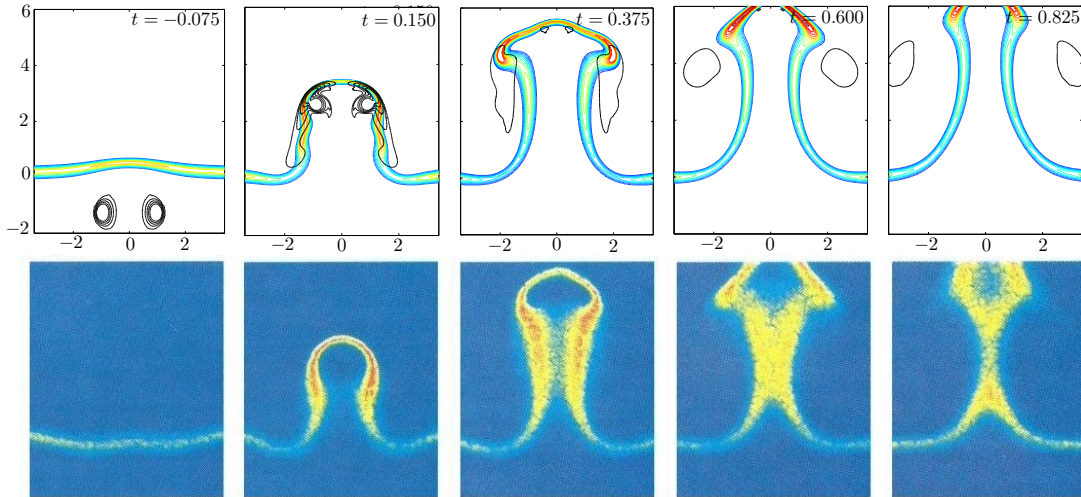
Figure 10: Top panel: numerical simulation of a strong flame with $Pe_0 = 30$, $\widetilde{\Gamma} = 40$ y $\mathcal{R} = 60$. Bottom panel: Fig. 12 of [57] (reprinted with permission from Elsevier).

Evolution of the number of elements and CPU times. All numerical simulations were run in a workstation with an Intel Core i7-3770k processor and $16\,\mathrm{GB}$ of DDR3 $1600\,\mathrm{MHz}$ RAM, compiled with the -O3 optimization flag using the GCC-4.7.3 compiler. The elapsed CPU time required to finish the $N_t = 1400$ time steps of the simulations for the three cases has been 65 minutes (Case 1), 103 minutes (Case 2) and 224 minutes (Case 3). As a summary of the three cases studied, we represent in Fig. 11 the evolution of the number of elements NE_n as a function of time. At the initial steps of the simulation, the vortex is still far away from the flame and we need a small number of elements to reproduce accurately both the vortex and the flame; in addition, during these initial instants, the case with the largest number of elements is that with the larger values of Pe_0, $\tilde{\Gamma}$, and $\mathcal{R}$. As soon as the vortex begins to interact with the flame ($t \sim 0$), we observe a growth in NE_n. The interaction between the vortex and the flame in Cases 1 and 2 is not as intense, and after a local extinction the number of elements stops growing and eventually starts to decrease. In Case 2, the number of elements starts to increase again around $t \sim 0.4$, reaching a maximum value at time $t \sim 0.5$ when the active flame front reignites the unburned mixture pocket that travels with the vortex. In Case 3, we have the most significant rise in the number of elements, due to the high robustness of the flame which now prevents its extinction, becoming instead extremely thin as it gets wrapped by the vortex. At later instants of the simulations, the number of elements decreases slowly due to the reduction of the vortex strength caused by viscous dissipation. The different degrees of anisotropy in the previous cases become evident though inspection of the maximum stretching factors; thus, the strong anisotropy of Case 3 shows a maximum streaching factor $\max(s_K) \sim 35$, whereas in Case 2, $\max(s_K) \sim 25$; finally, Case 1 presents a weakly anisotropic character with $\max(s_K) \sim 20$.
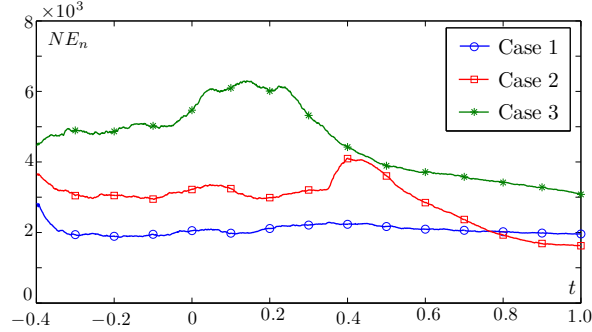
Figure 11: Evolution of number of elements NE_n for the three cases presented above for Test II. We use quadratic finite elements in anisotropic adaptive framework with tolerance $Tol = 1 \cdot 10^{-2}$.

Convergence results. Finally, we show in Table 3 the results for the global error $e_{L^2}(t_f)$ and each of the individual contributions (measured from the set of variables $\boldsymbol{\phi}$ (44) according to the definition (21)); we include the average number of elements $\overline{NE}$, and the tolerance Tol for each of the three cases of study, taking as the "reference" solution one computed using a very low tolerance $Tol = [0.5, 1, 2] \times 10^{-3}$ for Case 1, Case 2, and Case 3, respectively.

Table 3: Results for Cases 1-3 in Test II, using the anisotropic SLG scheme. Mean number of elements $\overline{NE}$, global L^2-error $e_{L^2}(t_f)$, and individual contributions.

Case 1, anisotropic SLG scheme in Test II

Tol	$\overline{NE}$	$e_{L^2}(t_f)$	$\beta_T e_{L^2}(T_f)$	$\beta_H e_{L^2}(Y_{Hf}))$	$\beta_u e_{L^2}(u_{xf})$	$\beta_u e_{L^2}(u_{yf})$
$2 \cdot 10^{-2}$	1406	0.090	0.0161	0.0161	0.0597	0.0634
$1 \cdot 10^{-2}$	2056	0.044	0.0064	0.0061	0.0297	0.0316
$5 \cdot 10^{-3}$	3131	0.024	0.0038	0.0039	0.0163	0.0172
$2 \cdot 10^{-3}$	5817	0.008	0.0012	0.0001	0.0055	0.0058

Case 2, anisotropic SLG scheme in Test II

Tol	$\overline{NE}$	$e_{L^2}(t_f)$	$\beta_T e_{L^2}(T_f)$	$\beta_H e_{L^2}(Y_{Hf}))$	$\beta_u e_{L^2}(u_{xf})$	$\beta_u e_{L^2}(u_{yf})$
$4 \cdot 10^{-2}$	1262	0.064	0.0462	0.0232	0.0299	0.0236
$2 \cdot 10^{-2}$	1841	0.030	0.0217	0.0120	0.0140	0.0101
$1 \cdot 10^{-2}$	2872	0.012	0.0085	0.0045	0.0060	0.0049
$5 \cdot 10^{-3}$	4702	0.005	0.0036	0.0019	0.0027	0.0021

Case 3, anisotropic SLG scheme in Test II

Tol	$\overline{NE}$	$e_{L^2}(t_f)$	$\beta_T e_{L^2}(T_f)$	$\beta_H e_{L^2}(Y_{Hf}))$	$\beta_u e_{L^2}(u_{xf})$	$\beta_u e_{L^2}(u_{yf})$
$8 \cdot 10^{-2}$	1273	0.170	0.1034	0.0692	0.0862	0.0770
$4 \cdot 10^{-2}$	1823	0.092	0.0554	0.0376	0.0480	0.0415
$2 \cdot 10^{-2}$	2791	0.044	0.0265	0.0180	0.0225	0.0193
$1 \cdot 10^{-2}$	4571	0.019	0.0114	0.0075	0.0100	0.0083

The estimated convergence rate $\widehat{\alpha}$ (using linear regression) of the global error with the average number of elements, $e_{L^2}(T) \propto \overline{NE}^{-\alpha}$ is computed and plotted in Figure 12. Here, although the convergence rates are lower than in the previous test owing to the much more complex character of the simulations and chemical model employed, the algorithm still performs quite satisfactorily, with $\widehat{\alpha} \sim 2.0$ and well-balanced contributions to the global error (see Table 3).

We have just examined three different diffusion flame/vortex interaction cases. For a more detailed account of the rich variety of interaction regimes arising from this problem, the reader
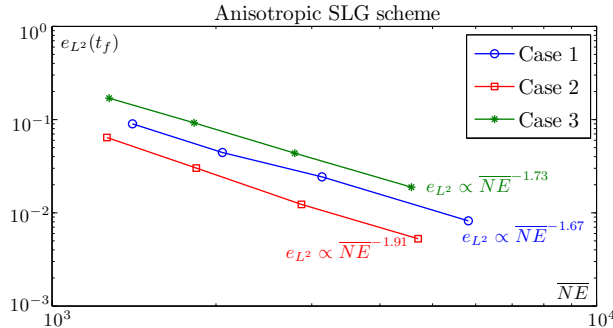
27

Figure 12: Convergence in the L^2-norm of the global error corresponding to Test II simulated using the local anisotropic adaptive semi-Lagrange-Galerkin scheme.

is referred to the recent review by Liñán et al. [56], where further results computed with our numerical method are discussed.

4. Conclusions

In this work we have presented a novel, local anisotropic, space-adaptive, finite element method for the simulation of unsteady combustion problems at low Mach and moderately high Reynolds numbers (i.e., under laminar flow conditions). The equations governing these phenomena are the Navier-Stokes equations supplemented by the energy and species mass conservation equations, the solution of which is accomplished by means of a mixed Lagrangian-Eulerian (or semi-Lagrangian) scheme: the convective terms are treated in the Lagrangian stage, whereas the Eulerian stage deals with the diffusion-reaction part of the equations. In addition, two different techniques have been considered for the Lagrangian stage, namely the classical semi-Lagrangian (SL) interpolation method, and the more accurate, semi-Lagrange-Galerkin (SLG) projection technique.

It has been shown that the semi-Lagrangian scheme effectively decouples the Navier-Stokes equations from the thermochemical problem (involving energy and species mass conservation), translating the former into a linear Stokes problem and the latter into a parabolic problem that can be tackled via an explicit Runge-Kutta-Chebyshev scheme which allows to compute all the thermodynamical variables of the problem separately; an explicit treatment that paves the way for a future full-parallelization of the numerical code. The time-marching method is embedded into an anisotropic, adaptive, finite element scheme which allows for an accurate and efficient representation of features such as boundary layers, mixing layers, or flame fronts. The adaptive refinement algorithm is controlled by a metric tensor built as the intersection of individual metric tensors with an a posteriori error indicator computed from the information supplied by the dominant convection terms.

To validate the code and illustrate the accuracy and efficiency of the numerical procedure, we choose a canonical combustion problem: the flame/vortex interaction. First we solve a planar, 2D premixed methane/air configuration replicating the results obtained by Lessani et al. [10]. We compare our results using uniform, isotropic, and anisotropic refinement, along with either the classical SL scheme or the SLG method; the SLG proves superior to the SL scheme under all circumstances. Then, to underscore the benefits of using anisotropic adaptation, we consider a flame/vortex interaction featuring stronger anisotropic features.

After the numerical validation of the code, we use our "workhorse technique", i.e., the anisotropic, semi-Lagrange-Galerkin scheme, to integrate the combustion equations in a more complex scenario: the non-premixed hydrogen-air flame/vortex interaction, modeled using

28

state-of-the-art descriptions for the molecular transport and the chemical-kinetics of hydrogen-air combustion. We have illustrated the rich phenomenology of such flame/vortex interactions with three different cases: weak flames with global extinction; more robust flames that suffer axial extinction followed by re-ignition; and very robust flames undergoing no extinction. At each and every situation, we observe an excellent agreement with laboratory experiments, and report the good convergence rates achieved by our numerical scheme.

Although far from perfect, the method presented in this paper has been shown to perform well in a selection of combustion problems, and has provided further insight into the complex behavior of flame/vortex interactions. However, we think that it may still benefit from research on a posteriori error analysis, interface discretization techniques, and a more efficient solution of the algebraic systems, topics that we intend to address in future works.

5. Acknowledgments

References

[1] F.A. Williams, Combustion Theory, 2nd ed, Addison-Wesley, Redwood City, 1985.

[2] S.B. Pope, Turbulent Flows, Cambridge University Press, UK (2000).

[3] N. Peters, Turbulent Combustion, Cambridge University Press, UK (2000).

[4] A. Liñán, F.A. Williams, Fundamental Aspects of Combustion, Oxford Univ. Press, New York, 1993.

[5] J. Buckmaster, P. Clavin, A. Liñan, M. Matalon, N. Peters, G. Sivashinsky, F.A. Williams, Combustion theory and modeling, P. Combust. Inst. 30(1) (2005) 1–19.

[6] M.D. Smooke, The computation of laminar flames, P. Combust. Inst. 34(1) (2013) 65–98.

[7] T. Poinsot, D. Veynante, Theoretical and Numerical Combustion, RT Edwards, Inc., 2005.

[8] H.N. Najm, P.S. Wyckoff, O.M. Knio, A semi-implicit numerical scheme for reacting flow: I. Stiff chemistry, J. Comput. Phys. 143 (1998) 381–402.

[9] B.A.V. Bennett, M.D. Smooke, Local rectangular refinement with application to non-reacting and reacting fluid flow problems, J. Comput. Phys. 151 (1999) 684–727.

[10] B. Lessani, M.V. Papalexandris, Time-accurate calculation of variable density flows with strong temperature gradients and combustion, J. Comput. Phys. 212 (2006) 218–246.

[11] C. Safta, J. Ray, H.N. Najm, A high-order low-Mach number AMR construction for chemically reacting flows, J. Comput. Phys. 229(24) (2010) 9299–9322.

[12] A.G. Tomboulides, J.C.Y. Lee, S.A. Orszag, Numerical simulation of low mach number reactive flows, J. Sci. Comput. 12(2) (1997) 139–167.

[13] R.B. Pember, L.H. Howell, J.B. Bell, P. Colella, W.Y. Crutchfield, W.A. Fiveland, J.P. Jessee, An adaptive projection method for unsteady, low-Mach number combustion, Combust. Sci. Technol. 140 (1998) 123–168.

[14] O. Filippova, D. Hänel, A novel lattice BGK approach for low Mach number combustion, J. Comput. Phys. 158 (2000) 139–160.

[15] S. Paolucci, Z.J. Zikoski, D. Wirasaet, WAMR: An adaptive wavelet method for the simulation of compressible reacting flow. Part I. Accuracy and efficiency of algorithm, J. Comput. Phys. 272 (2014) 814–841.

[16] D.J. Estep, M.G. Larson, R.D. Williams, Estimating the Error of Numerical Solutions of Systems of Reaction-Diffusion Equations, American Mathematical Soc., Vol. 696, 2000.

[17] M. Braack, An adaptive finite element method for reactive flow problems, Ph.D. thesis, University of Heidelberg, Heidelberg, Germany, 1998.

[18] R. Becker, M. Braack, R. Rannacher, Numerical simulation of laminar flames at low Mach number by adaptive finite elements, Combust Theor. Model. 3(3) (1999) 503–534.

[19] R. Becker, R. Rannacher, An optimal control approach to a posteriori error estimation in finite element methods, Acta Numerica 2001, in: A. Iserles (Ed.), Cambridge University Press, 2001.

[20] E. Burman, A. Ern, V. Giovangigli, An adaptive finite element method with crosswind diffusion for low Mach, steady, laminar combustion, J. Comp. Phys. 188(2) (2003) 472–492.

[21] E. Burman, A. Ern, V. Giovangigli, Bunsen flame simulation by finite elements on adaptively refined, unstructured triangulations, Combust. Theor. Model. 8(1) (2004) 65–84.

[22] M. Braack, T. Richter, Stabilized finite elements for 3-d reactive flows, Int. J. Numer. Math.Fluids. 51 (2006) 981–999.

[23] R. Bermejo, J. Carpio, A space-time element algorithm based on dual weighted residual methodology for parabolic equations, SIAM J. Sci. Comput. 31 (2009), 3324–3355.

[24] A. Belme, A. Dervieux, F. Alauzet, Time accurate anisotropic goal-oriented mesh adaptation for unsteady flows, J. Comput. Phys. 231(19) (2012) 6323–6348.

[25] B. Michaelis, B. Rogg, FEM-simulation of laminar flame propagation. I: Two-dimensional flames, J. Comp. Phys. 196(2) (2004) 417–447.

[26] B. Michaelis, B. Rogg, FEM-simulation of laminar flame propagation. II: Twin and triple flames in counterflow, Combust. Sci. Technol. 177(5–6) (2004) 955–978.

[27] P. Opiola, High-quality real-time simulation of a turbulent flame, in: Computational Science and Its Applications-ICCSA, Springer Berlin Heidelberg, 2011, pp. 112–122.

[28] M. Ainsworth, J.T. Oden, A Posteriori Error Estimation in Finite Element Analysis, John Wiley & Sons, 2000.

[29] P.J. Frey, F. Alauzet, Anisotropic mesh adaptation for CFD computations, Comput. Method. Appl. Mech. Eng. 194 (2005) 5068–5082.

[30] T. Coupez, G. Jannoun, N. Nassif, H.C. Nguyen, H. Digonnet, E. Hachem, Adaptive time-step with anisotropic meshing for incompressible flows, J. Comput. Phys. 241 (2013) 195–211.

[31] R. Bermejo, J. Carpio, An adaptive finite element semi-Lagrangian Runge-Kutta-Chebychev method for convection dominated reaction-diffusion problems, Appl. Numer. Math. 58 (2008) 16–39.

[32] A. Bermúdez, J.L. Ferrín, A. Liñán, L. Saavedra, Numerical simulation of group combustion of pulverized coal, Combust. Flame 158(9) (2011) 1852–1865.

[33] A. Allievi, R. Bermejo, Finite element modified method of characteristics for Navier-Stokes equations, Int. J. Numer. Meth. Fl. 32 (2000) 439–464.

[34] J. Carpio, J.L. Prieto, An anisotropic, fully adaptive algorithm for the solution of convection dominated equations with semi-Lagrangian schemes, Comput. Method. Appl. Mech. Eng. 273 (2014) 77–99.

[35] K.W. Morton, A. Priestley, E. Süli, Stability of the Lagrange-Galerkin method with non-exact integration, ESAIM-Math. Model. Num. (1988) 22(4) 625–653.

[36] O. Pironneau, On the transport-diffusion algorithm and its applications to the Navier-Stokes equations, Numer. Math. 38(3) (1982) 309–332.

[37] R. Bermejo, J. Carpio, A semi-Lagrange-Galerkin projection scheme for convection equations, IMA J. Numer. Anal. 30(3) (2010) 799–831.

[38] R. Bermejo, P. Galán del Sastre, L. Saavedra, A second order in time modified Lagrange-Galerkin finite element method for the incompressible navier-stokes equations, SIAM J. Numer. Anal. 50(6) (2012) 3084–3109.

[39] C.J. Mueller, J.F. Driscoll, D.L. Reuss, M.C. Drake, M.E. Rosalik, Vorticity generation and attenuation as vortices convect through a premixed flame, Combust. Flame 112(3) (1998) 342–346.

[40] T. Poinsot, D. Veynante, S. Candel, Quenching processes and premixed turbulent combustion diagram, J. Fluid Mech. 228 (1991), 561–606.

[41] J.C. Rolon, F. Aguerre, S. Candel, Experiments on the interaction between a vortex and a strained diffusion flame, Combust. Flame 100(3) (1995) 422–429.

[42] V.S. Santoro, D.C. Kyritsis, A. Liñán, A. Gomez, Vortex-induced extinction behavior in methanol gaseous flames: a comparison with quasi-steady extinction, P. Combust. Inst., 28(2) (2000) 2109–2116.

[43] M. Hermanns, M. Vera, A. Liñán, On the dynamics of flame edges in diffusion-flame/vortex interaction, Combust. Flame 149 (2007) 32–48.

[44] P.H. Renard, D. Thevenin, J. C. Rolon, S. Candel, Dynamics of flame/vortex interactions, Prog. Energy Combust. 26 (2000) 225–282.

[45] A. Allievi, R. Bermejo, A generalized particle search-locate algorithm for arbitrary grid, J. Comput. Phys. 132 (1997) 157–166.

[46] B.P. Sommeijer, L.F. Shampine, J.G. Verwer, RKC: An explicit solver for parabolic PDEs, J. Comput. Appl. Math. 88(2) (1998) 315–326.

[47] J.G. Verwer, B. Sommeijer, W. Hundsdorfer, RKC time-stepping for advection-diffusion-reaction problems, J. Comput. Phys. 201(1) (2004) 61–79.

[48] E.J. Dean, R. Glowinsky, On some finite elements methods for the numerical simulation of incompressible viscous flow, in: M.D. Gunzburger, R.A. Nicolaides (Eds.), Incompressible Computational Fluid Dynamics: Trends and Advances, Cambridge University Press, Cambridge, 1993, pp. 17–66.

[49] T. Coupez, Metric construction by length distribution tensor and edge based error for anisotropic adaptive meshing, J. Comput. Phys. 230(7) (2011) 2391–2405.

[50] W. Huang, Metric tensors for anisotropic mesh generation, J. Comput. Phys. 204 (2005) 633–665.

[51] J. Carpio, J.L. Prieto, R. Bermejo, Anisotropic "goal-oriented" mesh adaptivity for elliptic problems, SIAM J. Sci. Comput. 35(2) (2013) A861–A865.

[52] E.H. Georgoulis, E. Hall, P. Houston, Discontinuous Galerkin methods for advection-diffusion-reaction problems on anisotropically refined meshes, SIAM J. Sci. Comput. 30(1) (2007) 246–271.

[53] S. Giani, P. Houston, Anisotropic hp-adaptive discontinuous Galerkin finite element methods for compressible fluid flows, Int. J. Numer. Anal. Mod. 9(4) (2012) 928–949.

[54] K.A. Cliffe, J. Collins, P. Houston, Goal-Oriented a posterior error estimation for the travel time functional in porous media flows, SIAM J. Sci. Comput. 37(2) (2015) B127–B152.

[55] F. Hecht, BAMG: Bidimensional Anisotropic Mesh Generator, INRIA-Rocquencourt, France, 2006, `http://http://www.ann.jussieu.fr/hecht/ftp/bamg/`

[56] A. Liñán, M. Vera, A.L. Sánchez, Ignition, liftoff, and extinction of gaseous diffusion flames, Annu. Rev. Fluid. Mech. 47 (2015) 293–314.

[57] P.H. Renard, J.C. Rolon, D. Thevenin, S. Candel, Investigations of heat release, extinction, and time evolution of the flame surface for a non-premixed flame interacting with a vortex, Combust. Flame 117 (1999) 189–205.

[58] M. Vera, A. Liñán, On the interaction of vortices with mixing layers, Phys. Fluids 16(7) (2004) 2237–2254.

[59] R.M. Fristrom, L. Monchick, Two simple approximations to the thermal diffusion factor and their applications to flame studies, Combust. Flame 71(1) (1988) 89–99.

[60] R.J. Kee, F.M. Rupley, J.A. Miller, M.E. Coltrin, J.F. Grcar, E. Meeks, H.K. Moffat, A.E. Lutz, G. Dixon-Lewis, M.D. Smooke, J. Warnatz, G.H. Evans, R.S. Larson, R.E. Mitchell, L.R. Petzold, W.C. Reynolds, M. Caracotsios, W.E. Stewart, P. Glarborg, CHEMKIN Collection, Release 3.5, Reaction Design, Inc., San Diego, CA, 1999.

[61] G.P. Smith, D.M. Golden, M. Frenklach, N.W. Moriarty, B. Eiteneer, M. Goldenberg, C.T. Bowman, R.K. Hanson, S. Song, W.C. Gardiner, V.V. Lissianski, Z. Quin, GRI-Mech 3.0, 1999, `http://combustion.berkeley.edu/gri_mech/data/nasa_plnm.html`

[62] A.L. Sánchez, F.A. Williams, Recent advances in understanding of flammability characteristics of hydrogen, Prog. Energy Combust. 41 (2014) 1–55.

[63] P. Boivin, C. Jiménez, A.L. Sánchez, F.A. Williams, An explicit reduced mechanism for H_2-air combustion, P. Combust. Inst. 33(1) (2011) 517–523.

[64] P. Saxena, F.A. Williams, Testing a small detailed chemical-kinetic mechanism for the combustion of hydrogen and carbon monoxide, Combust. Flame 145 (2006) 316–323.